Site-Specific Texture and Its Influence on Mechanical Behavior in Direct Energy Deposited Ti-6Al-4V Walls

Rajib Halder[a], Arjun Mahato[b], Souvik Sahoo[c], Jake T. Benzing[d], Shibayan Roy[b], Anthony D. Rollett[a,*]

[a]*Materials Science and Engineering, Carnegie Mellon University, Pittsburgh, PA, 15213 USA*

[b]*Indian Institute of Technology, Kharagpur, WB, India*

[c]*IMDEA Materials Institute, Madrid, 28906 Spain*

[d]*National Institute of Standards and Technology, Boulder, CO, 80305 USA*

Abstract

Laser hot wire direct energy deposited (LHW-DED) Ti-6Al-4V wall structures experience variable cooling rates along the build direction as heat accumulates with wall height. These variations in thermal history affect the microstructure, texture, and texture-mediated mechanical response within the walls. In the present work, site-specific texture in single- and multi-walled specimens and its concomitant effect on the localized mechanical properties are investigated via large-scale EBSD characterization and a polycrystal plasticity model based on the viscoplastic self-consistent (VPSC) framework. The effect of secondary process parameters, viz. interlayer delay and scan strategy, on the texture evolution was also examined. The results revealed that the transformed α and (prior) β texture intensities simultaneously increase with increasing wall height. The reconstructed parent β grain structure exhibits a strong cube texture with two α fibers, namely $\langle 01\bar{1}2\rangle_\alpha$ and $\langle 11\bar{2}0\rangle_\alpha$ aligned parallel to the build direction in both single- and

*Corresponding author.
E-mail address: rollett@andrew.cmu.edu

multi-walled specimens. VPSC simulations revealed the role of site-specific texture in the tensile properties and anisotropic mechanical behavior of the walls.
Keywords: Ti-6Al-4V, Laser Hot Wire Direct Energy Deposition, Wall Structure, Site-specific Texture, Mechanical Properties

1. Introduction

Additive manufacturing (AM) of metal parts involves layer-by-layer deposition to produce near-net shape components with desired properties. In laser hot wire direct energy deposition (LHW-DED) technique, the preheated wire is fed into the high energy laser spot to melt and deposit simultaneously [1, 2]. The high energy density coupled with high deposition rate in layer-wise deposition gives rise to heat accumulation with increasing build height. This in turn introduces differential thermal gradients along the build height in the as-fabricated components [3]. This temperature heterogeneity along the build direction causes Ti-6Al-4V alloy (Ti64) to undergo a complex microstructural evolution in LHW-DED processing that in turn leads to heterogeneous mechanical properties in as-built components [4, 5]. The slower cooling rates in LHW-DED, unlike laser powder bed fusion (LPBF), typically lead to the formation of a lamellar $\alpha + \beta$ (Widmanstätten) microstructure rather than a fully martensitic α' structure [6, 7].

During solidification, prior β phase grains grow epitaxially across layers, forming columnar grains aligned with the build direction [8, 9, 10, 11]. This behavior arises since each newly deposited layer partially remelts the previous one, thereby eliminating nucleation barriers and promoting grain growth on pre-existing structures [12]. As a result, the long columnar β grains develop $\langle 100 \rangle \parallel$ BD fiber texture in accordance with the thermal gradient and heat extraction. This is to say, the β grains tend to align their $\langle 100 \rangle$ direction with the heat flow because of the fast and easy growth of the $\langle 100 \rangle$ direction for a cubic crystal structure during solidification [13, 14]. Upon transformation

to α phase, Burgers orientation relationship (BOR) results in α variants inheriting the geometrically parallel orientations of the prior β phase, producing a α texture linked to the original β structure [15, 16, 17, 18]. However, LHW-DED Ti64 parts often exhibit spatial variations in texture, which introduce mechanical anisotropy and may degrade component performance in service [19, 20, 21, 22, 23].

Several studies have investigated different additive manufacturing processes influencing microstructure and texture evolution for Ti64 alloy. For instance, Waryoba *et al.* [6] conducted a comparative electron backscatter diffraction (EBSD) analysis of Ti64 produced via laser and electron beam (EB) DED. Near the substrate, both processes resulted in a weak or negligible texture due to widespread nucleation. As the EB DED build advanced, strong microtexture and pronounced variant selection developed. This trend suggested that variant selection intensified under repeated thermal cycling. In contrast, laser DED maintained a weak texture throughout the build, likely due to smaller β grains and greater melt pool disturbance, both of which limited the development of a dominant orientation. Baufeld *et al.* [24] demonstrated that in single-pass laser-deposited walls, β grains initially grew along $\langle 100 \rangle$ but gradually tilted as the wall grew due to changes in the heat flow direction, leading to a spatial gradient in texture. Similarly, Sahoo *et al.* [25] observed columnar prior-β grains extending along the build direction in Ti64 walls produced using LENS. The resulting α phase formed basket-weave colonies, whose orientations were not random but inherited from the prior β phase.

Neutron diffraction studies have provided further insight into bulk texture development. Pesach *et al.* [26] found that wire-arc DED produced extremely sharp $(0001)_\alpha$ textures, significantly stronger than those seen in LPBF. Neikter *et al.* [27] reported the strongest textures generated via wire DED among the AM processes examined. They also observed higher α texture intensity near the base of the build, where a steep thermal gradient enabled early dominance of a single orientation, while upper regions exhibited

reduced texture intensity due to more uniform thermal conditions.

In LPBF processing, scan strategy plays a key role in shaping site-specific textures. A unidirectional scan path promotes β grain alignment along both the scan and build directions [12]. Alternating the hatch pattern between layers, such as rotating by 90° or 67°, randomizes in-plane β grain orientations and encourages their vertical growth along BD. Al-Bermani *et al.* [13] showed that 90° rotations led to a more randomized $\langle 100 \rangle_\beta$ texture resembling a cube texture. Thin-walled structures, which cool more rapidly in the lateral direction, can exhibit β grains aligned perpendicular to the wall, *i.e.* with respect to BD, resulting in tilted or bi-modal $\langle 100 \rangle \parallel$ BD orientations. While island scan strategies reduce global texture, macrozones — *i.e.* the clusters of α grains sharing similar orientation — can still develop in regions with consistent thermal histories.

Texture variation has also been observed in electron beam melting (EBM) through different scan strategies. Saville *et al.* [28] compared point-melt and raster modes to report that point-melt scans produced finer microstructures but stronger α texture. These AM structures transitioned from Widmanstätten to lamellar α colony with build height ultimately resulting in an increasing α texture intensity. Raster scans, by contrast, formed α' martensite that decomposed into fine acicular α lamellae, producing weaker α texture. Neutron diffraction confirmed that all strategies resulted in some degree of α fiber texture, but raster scans produced the weakest. Contour and hatch scanning strategies in EBM also influenced local α texture near the part surface. Antonysamy *et al.* [14] found that thick EBM builds contained β grains spanning the full build height and aligned $\langle 100 \rangle$ with the build direction, while thinner regions exhibited grain tilting. They also noted that part rotation or geometry adjustments can significantly influence grain orientations. Although standard EBM practice involves a zigzag scan pattern with 90° rotation per layer, this approach still results in a fiber texture. However, Al-Bermani *et al.* [13] reported that zigzag scanning led to a β texture ten times more random than with fixed-direction

scanning due to high build temperatures and extended thermal cycles.

Although the above-mentioned studies provide insight into the site-specific variation of microstructure and texture in Ti64 parts fabricated by powder-based additive manufacturing techniques, limited studies so far had reported the same for wire-based AM-processing. Since the degree of heat accumulation in LHW-DED process is relatively high due to the slower cooling rate and higher deposition rate than powder-based AM techniques, significantly higher differential cooling rates with increasing build height are expected for the as-deposited LHW-DED parts. This may in turn give rise to pronounced microstructural coarsening as well as location-specific variation in microtexture evolution and orientation-mediated mechanical anisotropy, especially for thin-walled Ti64 components. It is therefore imperative to investigate site-specific texture evolution and its influence on the degree of mechanical anisotropy for as-built Ti64 parts.

To this end, location-specific microtexture evolution with respect to the build height was studied for transformed α and prior β phases for the case of a fifteen layer tall single-bead wall (SW) and another with five layer wide and twelve layer tall multi-bead wall (MW) Ti64 parts with either distinct interlayer delays (for SW) or varying scan strategies (for MW). This is so done since the heat build-up and consequently, the thermal gradients is controlled through the interlayer delay between deposition of successive layers and by implementing different scan strategies. The present study therefore explores the influence of interpass dwell time and scan strategies on the microtexture evolution of as-deposited Ti64 parts. Uniaxial tensile tests were conducted to examine the orientation-induced anisotropy wherein specimens were extracted at different directions relative to the build direction. Subsequently, a polycrystal plasticity based viscoplastic self-consistent (VPSC) model was developed to assess the influence of site-specific texture on the mechanical properties at different build heights. Since the developed VPSC model did not use microstructural information as input, rather only uses the texture data from different

build heights, it allows for deconvolution of effects from microtexture and microstructure evolution on the mechanical properties.

2. Experimental Procedure

Ti64 SW specimens with three different interlayer delays of 0 (SW1), 120 (SW2), and 300 (SW3) s were fabricated using LHW-DED process while another set of MW Ti64 specimens was fabricated with different scanning strategies (MW1, MW2, and MW3). Note that the nominal delays are in addition to the inherent gap of $\approx 8\ s$. The processing parameters for the fabrication of single and multi- wall specimens are provided in Table 1. Figures 1a & 1b exhibit images of Ti64 SW and MW specimens built in the present study. The detailed scan strategies employed to fabricate the three MW specimens are also delineated in the Figure 1c. Further details about the LHW-DED process can be found in Ref. [3].

Table 1: The process parameters for the deposition of SW and MW specimens in LHW-DED

Process Parameters	SW1	SW2	SW3	MW1	MW2	MW3
Laser Power (W)	5000	5000	5000	4500	4500	4500
Wire Power (W)	300	300	300	200	200	200
Feed Rate (mm/s)	57.5	57.5	57.5	40	40	40
Scan Speed (mm/s)	5	5	5	5	5	5
Interlayer Delay (s)	0	120	300	0	0	300 after 3V layers
Scan Strategy	-	-	-	Left to Right	Inside Out	Left to Right (3V)/ Right to Left (3V)
Hatch Spacing (mm)	-	-	-	6.19	6.19	6.19
No. of Beads	15V	15V	15V	5H/12V	5H/12V	5H/12V
Energy Density (J/mm^3)	70	70	70	70	70	70

V=Vertical; H=Horizontal

Energy Density= (laser power + wire power)/(speed x bead height x hatch spacing (or spot size for single track wall) [29])

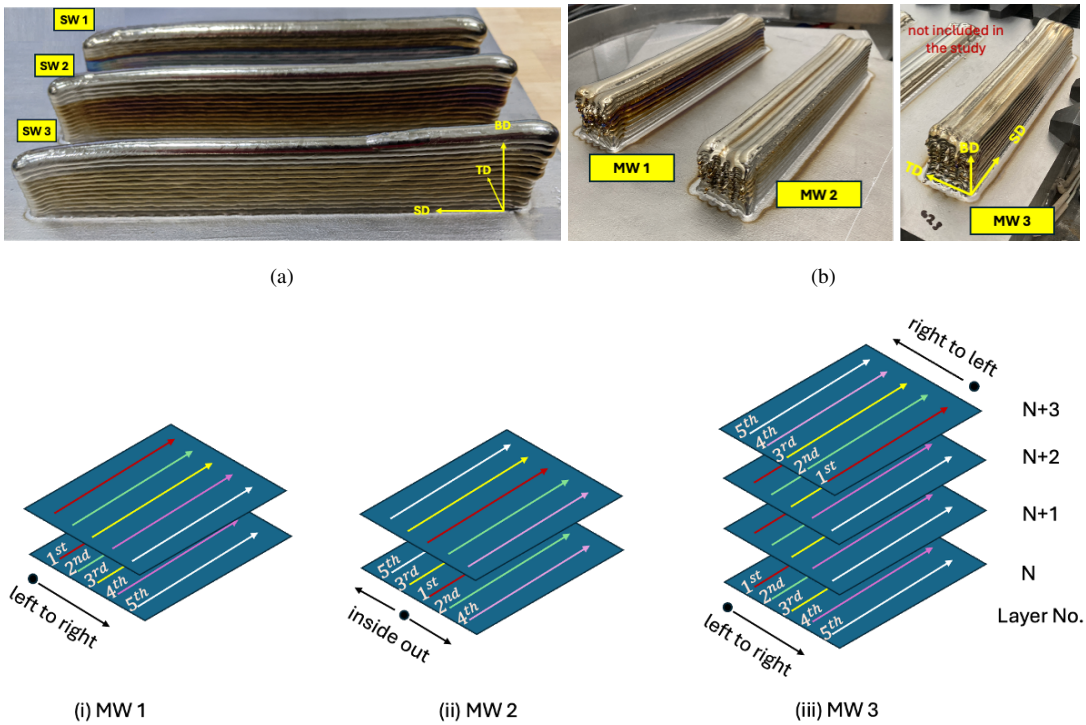

Figure 1: Macro-images (not to scale) illustrating (a) SW and (b) MW specimens in the as-built conditions; (c) Schematic diagram demonstrating the distinct scan strategies employed to fabricate MW specimens. The sequence of laser scans for different layers is also delineated.

2.1. Microtexture Analysis

SW and MW Ti64 specimens were sectioned using electric discharge machining (EDM) and subsequently polished [30] for electron backscatter diffraction (EBSD) characterization at room temperature using a LEO 1525 field emission scanning electron microscope (FESEM) operating at an accelerating voltage of 25 kV and a working distance of 21 mm. EBSD data was acquired from regions marked by rectangular boxes in the lower and upper sections of the wall specimens, as shown in Figure 2a & 2b. In Figure 2a, the difference in wall height between SW1 and SW2/SW3 is attributed to heat accumulation in SW1 caused by the shortest interlayer delay, which progressively alters melt pool width and length and leads to geometric distortion. In contrast, the

longer interlayer delays in SW2 and SW3 dissipate heat more effectively, stabilize melt pool dimensions, and result in a more uniform wall geometry. Further analysis of heat accumulation effects on melt pool behavior is provided in our previous work [3]. A dynamic focus of 44.8 %, a step size of 4 μm, and 4×4 binning were used for EBSD data acquisition. For each specimen, 81 smaller EBSD maps (~1100 μm × 1100 μm) were initially collected and subsequently stitched to create a large-area map of approximately 10 mm × 10 mm, capturing the as-built microtexture. Additional details regarding the EBSD methodology can be found in Ref. [18].

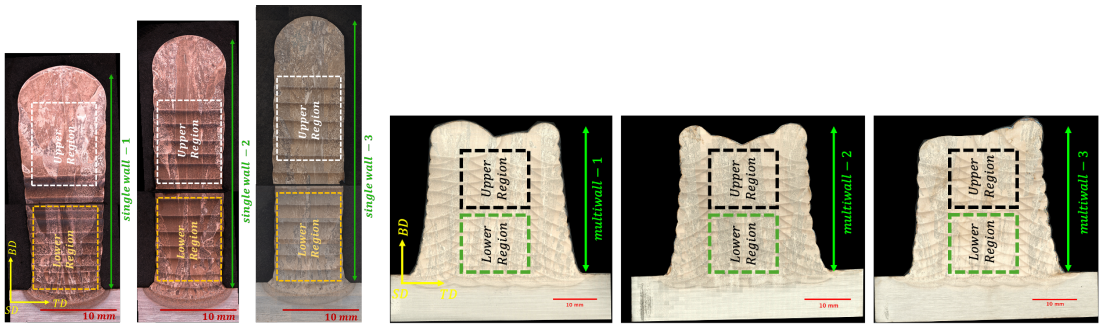

(a) (b)

Figure 2: Optical micrographs showing the cross-sections from (a) SW and (b) MW specimens. The annotated rectangular boxes highlight the area from which EBSD scans were collected for site-specific texture measurement. The build direction (BD), scan direction (SD), and transversal direction (TD) are also delineated in the figure.

The room-temperature EBSD data contain orientation information solely from the transformed α phase and were analyzed using TSL OIM software (version 8, EDAX Inc.) alongside the MTEX toolbox (v5.10) in MATLAB [31]. Reconstruction of the prior β-phase orientations was performed using MTEX in conjunction with the ORTools add-on library (v2.3.0) [32]. A consistent hexagonal axis convention was followed by aligning the build direction along the z-axis. Fiber volume and β grain size were measured from the combined EBSD maps taken from the lower and upper regions of the SW and MW specimens (Figure 2). Additional analyses were performed on smaller

regions cropped from the full EBSD maps, each representing approximately a single deposited layer. These regions were categorized as bottom, center, and top sections, corresponding to layers 1, 6, and 15 in the SW specimens and layers 1, 6, and 12 in the MW specimens. The location-specific texture was evaluated by comparing the texture strength across different sections of the wall. Here, texture strength is quantified as the square root of the texture index. The texture index, as defined by Bunge [33], is given by:

$$F^2 = \frac{1}{8\pi^2} \sum_i [f(g_i)]^2 \Delta g_i,$$

where $f(g_i)$ is the value of the orientation distribution function (ODF) at orientation g_i, and Δg_i is the corresponding orientation cell volume. The texture index is expressed in units of m.r.d.^{2} (multiples of a random distribution) and represents the mean square value of the ODF.

2.2. Tensile Tests

To evaluate the influence of crystallographic texture on the ensuing mechanical properties of the AM Ti64 alloy, tensile tests were performed at room temperature with a strain rate of 0.1 mm/min on subsized tensile samples machined along various loading directions relative to BD of the SW parts. The dimensions of the tensile specimens and the specimen preparation scheme with reference to the SW part are illustrated in Figure 3.

In this study, tensile testing was conducted exclusively on SW specimens, as the primary objective was to use multi-directional tensile data to validate the VPSC crystal plasticity simulation model. Once validated, this model could be employed to investigate the influence of site-specific texture evolution on mechanical properties. Since SW and MW specimens exhibit comparable directional mechanical behavior, tensile data from the SW specimens alone were deemed sufficient for robust model validation.

**Certain commercial software, equipment, instruments or materials are identified in this paper to adequately specify the experimental procedure. Such identification is not intended to imply recommendation or endorsement by the National Institute of Standards and Technology, nor is it intended to imply that the equipment or materials identified are necessarily the best available for the purpose*

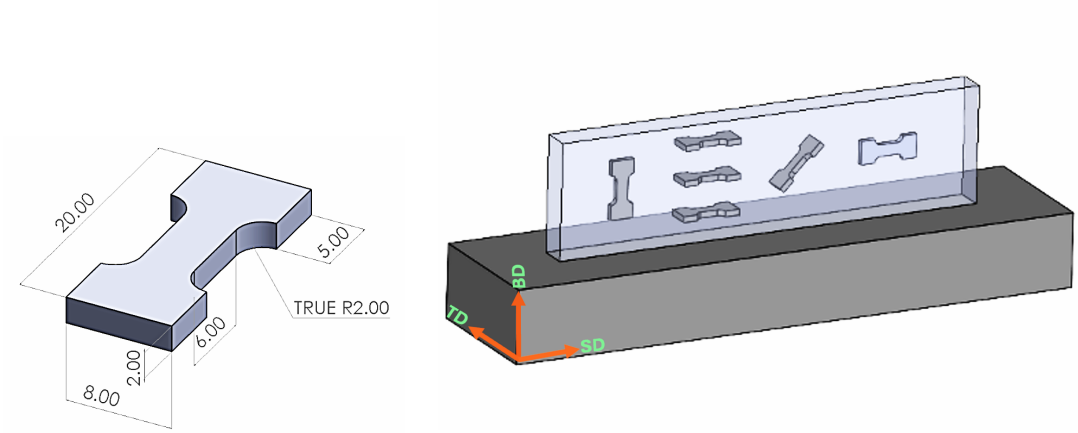

(a) (b)

Figure 3: (a) Schematic illustrating the dimensions of the sub-sized tensile specimens; (b) Orientation of different tensile sample with respect to specimen coordinate directions. Tensile samples from left to right are labeled as vertical, horizontal$_1$, diagonal, and horizontal$_2$ tensile specimens.

2.3. Polycrystal Plasticity Modeling

A polycrystal plasticity model based on Visco-Plastic Self-Consistent (VPSC) [34] formulation is developed here to predict the mechanical anisotropy of SW and MW specimens as a function of site-specific texture evolution. This model is convenient for isolating the effect of microtexture on the mechanical properties, as it represents any material system purely through sets of crystallographic orientations to represent the texture, without incorporating explicit microstructural details.

VPSC simulation calculates the mechanical behavior of a polycrystal by establishing a two-way interaction between individual constituent grains wherein the polycrystal is considered as a homogeneous effective medium (HEM), *i.e.* a matrix [34, 35, 36]. Each grain is then treated as a visco-plastic, anisotropic ellipsoidal inclusion embedded within the HEM which enables local deviations between the microscopic (grain-level) and macroscopic (polycrystal-level) stress and strain rate. “Hard” grains can deform less than the average and vice versa. The macroscopic behavior is constrained to satisfy the

boundary conditions on overall stress and strain rate of the polycrystal.

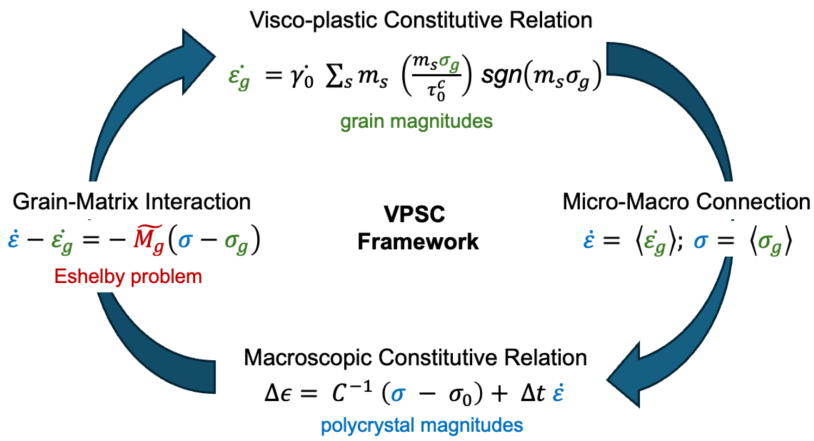

Figure 4: Visco-plastic self-consistent framework illustrating the two-way relationship between polycrystal and individual grains for calculation of stress and strain rate during deformation [37].

Additionally, the grain-matrix interaction equation in VPSC defines the relationship between the mechanical behavior of individual grains and the overall response of the HEM, by employing an Eshelby inclusion approach [38]. This method ensures that the stress and strain rate are uniform within each grain (inclusion) while being allowed to vary from the macroscopic averages. Solving the stress equilibrium equation for a visco-plastic (VP) inclusion embedded within a VP medium result in the formulation of the grain-matrix interaction equations. The mechanical response of the polycrystal must simultaneously satisfy the macroscopic mechanical behavior measured for a given material, while each grain follows the visco-plastic constitutive equation, discussed in the next paragraph. Together, these governing equations form the self-consistent framework illustrated in Figure 4. An iterative numerical algorithm is employed to converge on a solution for each strain step.

In the present study, the VPSC model used Voce hardening law at the individual slip

system level, with the initial texture as input. The initial values of the critical resolved shear stress (CRSS) for various slip systems were adopted from Galán-López *et al.* [39]. The strain hardening parameters, *i.e.,* τ_0, τ_1, θ_0, and θ_1, were optimized to fit the experimental curves while constraining the hardening parameters according to $\tau_0 > 0$, $\tau_1 > 0$, $\theta_0 > 0$, and $\theta_1 < 0$. A total of 24 slip systems were considered to simulate the deformation behavior of the primary α-phase. These include: three basal $(0001)\langle 11\bar{2}0\rangle$, three prismatic $(10\bar{1}0)\langle 11\bar{2}0\rangle$, six $\langle a\rangle$ first-order pyramidal $(10\bar{1}1)\langle 11\bar{2}0\rangle$, and twelve $\langle c+a\rangle$ first-order pyramidal $(10\bar{1}1)\langle 11\bar{2}3\rangle$ slip systems, as illustrated in Figure 5. To evaluate the accuracy of the model, the textures predicted after deformation from the VPSC simulations were compared with the experimental textures obtained from the post-fracture tensile specimens.

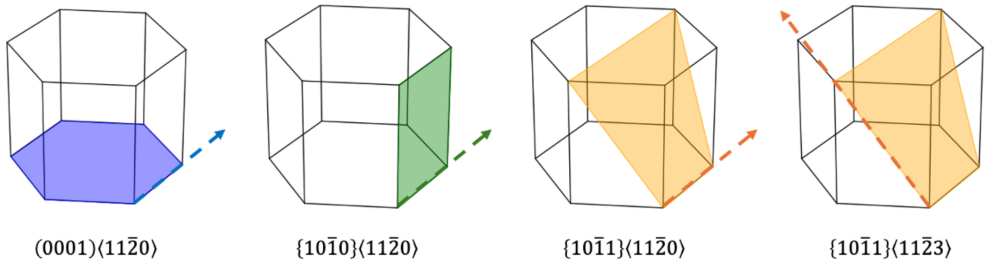

Figure 5: Different slip geometries of HCP α-phase of Ti64

3. Results

3.1. α Texture

Location-specific α texture was analyzed from the lower and upper regions of both SW and MW specimens using smaller (cropped) EBSD data, as illustrated in Figure 6a & 6b. The normal direction (ND) of the EBSD maps coincides with the BD. Similarly, $(0001)_\alpha$ and $(11\bar{2}0)_\alpha$ stereograms contain the BD at the center. The normal direction inverse pole figures (ND-IPFs) are plotted such that BD is parallel to ND. The $(0001)_\alpha$ and $(11\bar{2}0)_\alpha$ pole figures and ND-IPFs are employed to investigate the variation of texture

strength across the specimen height. The pole figures from the bottom, center, and top regions of the wall depicts increasing α texture strength with wall height in SW specimens. However, a clear trend of increasing texture intensity does not exist in MW specimens (Figure 7a). Furthermore, Figure 7a shows that the overall α-texture intensity is stronger in SW specimens than the MW samples. For example, the SW3 specimen showed texture strengths of 1.35, 1.84, and 2.15 m.r.d. in the bottom, center, and top sections, respectively, while the MW3 specimen exhibited maximum texture strengths of 1.40, 1.65, and 1.56 m.r.d. in the corresponding sections.

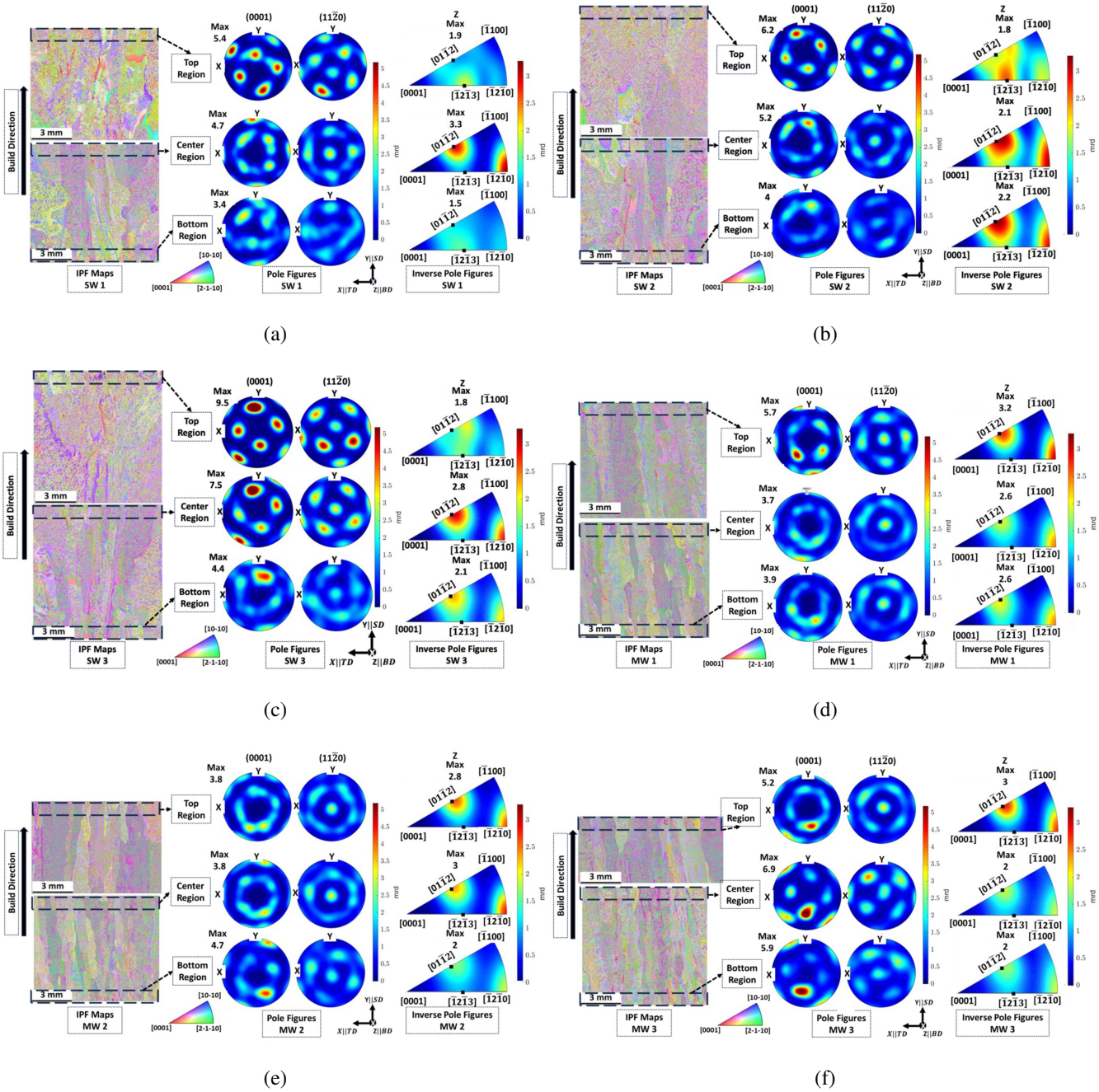

Figure 6: The ND || BD-IPF maps of α phase, (0001) and $(11\bar{2}0)$ stereograms, and ND || BD inverse pole figures from different wall heights for (a-c) SW and (d-f) MW specimens. The color coding for IPF maps is given alongside. The stereograms are plotted to align BD with the Z-axis, SD with Y-axis, and TD with X-axis of the specimen reference frame.

As shown in $(0001)_\alpha$ stereograms, basal poles are oriented within an angular range of 45–60° relative to the build direction, which lies at the center (Figure 6). A closer examination of $(0001)_\alpha$ and $(11\bar{2}0)$ pole positions across the bottom, center, and top regions reveals that they progressively tilt away from BD with increasing wall height. This can be attributed to the formation of columnar β grains resulting in a dominant $\{100\}$ || BD texture component due to the rapid growth along $\langle 100 \rangle$ direction during solidification [13, 6]. The preferential growth initially aligns closely with the maximum heat flow at the solid–liquid interface but tends to tilt away from the build direction as convective and radiative heat dissipation mechanisms become more significant with increasing wall height [40, 41]. The $(100)_\beta$ stereograms from reconstructed β grains in Figure 8 further confirm the tilting of $(100)_\beta$ poles away from the BD (along the ND *i.e.,* at the center) with increasing wall height.

The ND-IPFs in Figure 6 further illustrate the α texture with respect to the orientation of the build direction. In SW2 and SW3, the bottom and center regions display a BD || $\langle 01\bar{1}2 \rangle$ texture component, while the top region exhibits a BD || $\langle 11\bar{2}0 \rangle$ texture component. In SW 1, although BD || $\langle 01\bar{1}2 \rangle$ texture is prominent at the center region, the bottom and top regions are characterized by BD || $\langle 11\bar{2}0 \rangle$ texture. Overall, BD || $\langle 01\bar{1}2 \rangle$ texture is dominant in the SW specimens. In contrast, the MW specimens contain BD || $\langle 01\bar{1}2 \rangle$ texture consistently across all three regions (bottom, center, and top). Moreover, the maximum intensity of BD || $\langle 01\bar{1}2 \rangle$ component appears at the center region in case of SW specimens, while for MW specimens, it is at the top region regardless of the scan strategy (Figure 7b).

Location-dependent texture for SW and MW specimens indicate that an extended interlayer delay results in a comparatively higher texture intensity (SW3 > SW2 > SW1) in SW specimens (Figure 7a). This suggests that interlayer delay significantly affects the overall α texture intensity in AM Ti64 parts. In contrast, different scan strategies for

MW specimens appear to have minimal influence on the texture intensity (MW1 ≈ MW2 ≈ MW3).

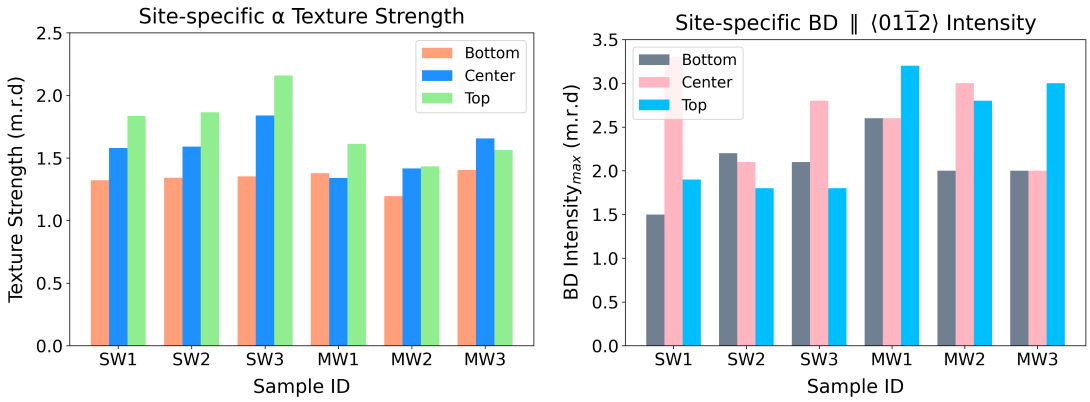

(a) (b)

Figure 7: (a) α-texture intensity between bottom, center, and top regions and (b) The variation in BD intensity in bottom, center, and top sections in SW and MW specimens.

3.2. *Prior β Texture*

The reconstructed prior β ND-IPF maps (ND ∥ BD) for both SW and MW specimens in Figure 8 reveal that a strong cube texture, *i.e.,* $\{001\}_\beta$ ∥ BD, forms in both SW and MW specimens. The epitaxial growth of columnar β grains opposite to the direction of heat flow into the baseplate causes such orientation development [8, 9, 10, 11]. However, small fractions of equiaxed β grains are also present near the deposited specimen-substrate interface at the bottom section. The dramatic coarsening reflected in the increase in β grain size occurs with increasing wall height, particularly in SW specimens. In the upper section, the β grains exhibit an outward bending toward the wall edges, which is not observed in case of MW specimens. This results from heat loss through the side surfaces of the wall by convection and radiation mechanisms.

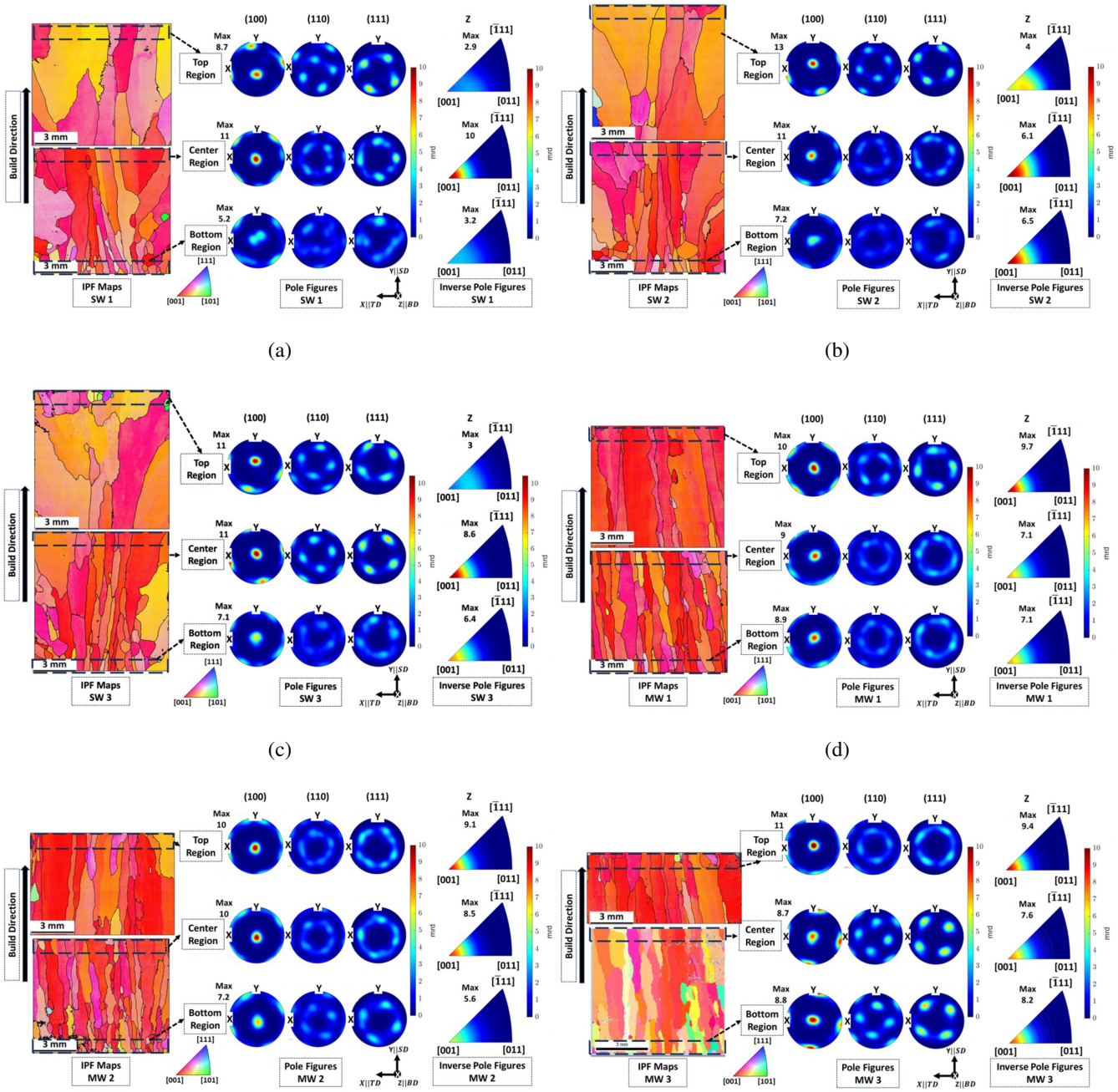

Figure 8: Reconstructed β $ND \parallel BD$ IPF maps, $(100)_\beta$, $(110)_\beta$, $(111)_\beta$ pole figures and inverse pole figures for Z-axis ($Z \parallel BD$) shown for both (a-c) SW and (d-f) MW specimens. The color coding for IPF maps and the axes convention used for stereograms are given alongside.

By comparing the locations of $(110)_\beta$ and $(0001)_\alpha$ poles as well as $(111)_\beta$ and $(11\bar{2}0)_\alpha$ poles in the respective stereograms , it can be confirmed that the BCC $\beta \rightarrow$ HCP α phase transformation in the SW and MW specimens maintains the Burgers orientation relationship (Figure 6 & 8). Figures 9a and 9b present the variation in β texture strength and the BD $\parallel$ $(100)_\beta$ texture component along the height of the SW and MW specimens. As shown in Figure 9a, the β texture strength increases with wall height in the SW specimens. In contrast, the MW specimens do not exhibit a clear trend in β texture intensity across the height. This site-specific evolution in β texture strength closely mirrors the trend observed in the α phase. Additionally, the overall β texture strength is greater in SW specimens compared to MW specimens. The ND-IPFs further indicate that the BD $\parallel$ $\langle 100 \rangle$ texture component is strongest at the center of the SW specimens, whereas in the MW specimens, it reaches its peak intensity at the top, as shown in Figure 9b.

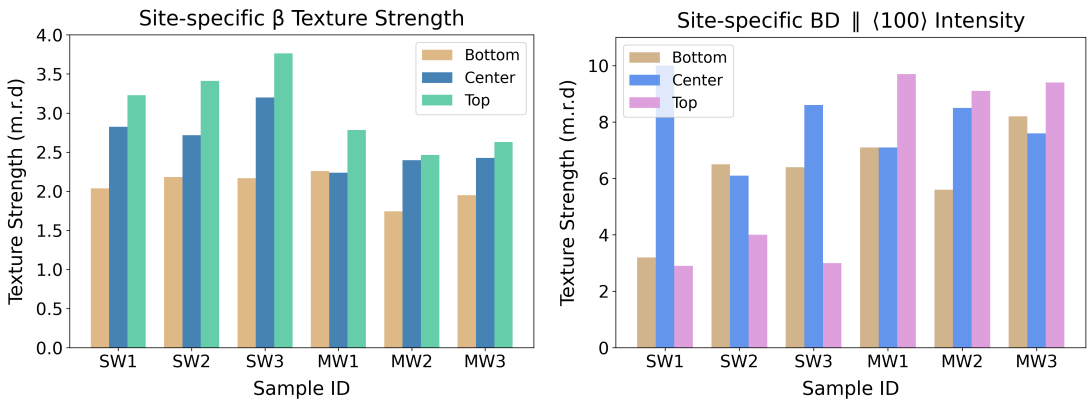

(a) (b)

Figure 9: The evolution of (a) site-specific β texture strength and (b) BD $\parallel$ $\langle 100 \rangle$ intensity with increasing wall height for SW and MW specimens.

3.3. Fiber Texture

A fiber texture is a crystallographic texture defined by the cylindrical symmetry of crystal orientations around a specific axis or direction in the sample. In such cases,

specific crystallographic directions (*e.g.,* $\langle 11\bar{2}0\rangle$ or $\langle 01\bar{1}2\rangle$) preferentially align with the uniaxial processing direction, *e.g.,* the build direction in AM while orientations are otherwise randomly distributed around that axis. In the present study, two distinct α fibers aligned along the BD in both SW and MW specimens. Figure 10 further represents the $\Phi = 0°$ sections of orientation distribution function (ODF) from the lower and upper regions of various SW and MW specimens highlighting the locations of fibers parallel to the BD. The primary fiber, $\langle 01\bar{1}2\rangle_\alpha$ is located at $\Phi \approx 42°$, whereas the secondary fiber, $\langle 11\bar{2}0\rangle_\alpha$ is positioned at $\Phi \approx 90°$. Previously, a fiber texture having BD $\parallel \langle 01\bar{1}2\rangle_\alpha$ was reported as the primary texture component in EBM-processed Ti64 components from neutron diffraction [28, 42, 26]. In the lower regions of both SW and MW specimens, a continuous $\langle 01\bar{1}2\rangle_\alpha$ fiber is evident, whereas in the upper regions, the fiber appears more discontinuous and fragmented.

The change in fiber intensity with the wall height was evaluated from the variation in fiber volume. The fiber volume fractions were quantified in MTEX using a 5° resolution orientation distribution function (ODF) and a 10° search radius centered on the build direction. Figure 11 suggests that $\langle 01\bar{1}2\rangle_\alpha$ is the primary fiber while $\langle 11\bar{2}0\rangle_\alpha$ appears in smaller volumes. In the SW specimens, the volume of $\langle 01\bar{1}2\rangle_\alpha$ is about twice that of $\langle 11\bar{2}0\rangle_\alpha$. In case of MW specimens, the former fiber is about 1.6 times higher in volume than the latter. The total fiber volume fraction is although greater in MW specimens than in SW ones. On average, the volume% of $\langle 01\bar{1}2\rangle_\alpha$ and $\langle 11\bar{2}0\rangle_\alpha$ fibers are approximately 15% and 7% in SW specimens, and approximately 19% and 11% in MW specimens. Moreover, in SW specimens, the fiber volume fractions of BD $\parallel \langle 01\bar{1}2\rangle_\alpha$ and BD $\parallel \langle 11\bar{2}0\rangle_\alpha$ decrease with the wall height. In contrast, they increase with wall height in MW specimens. However, no clear relationship exists between process variables like interlayer delay (*i.e.,* between SW1, SW2, & SW3) and scan strategies (*i.e.,* between MW1, MW2, & MW3) and the fiber volume fractions along the build direction.

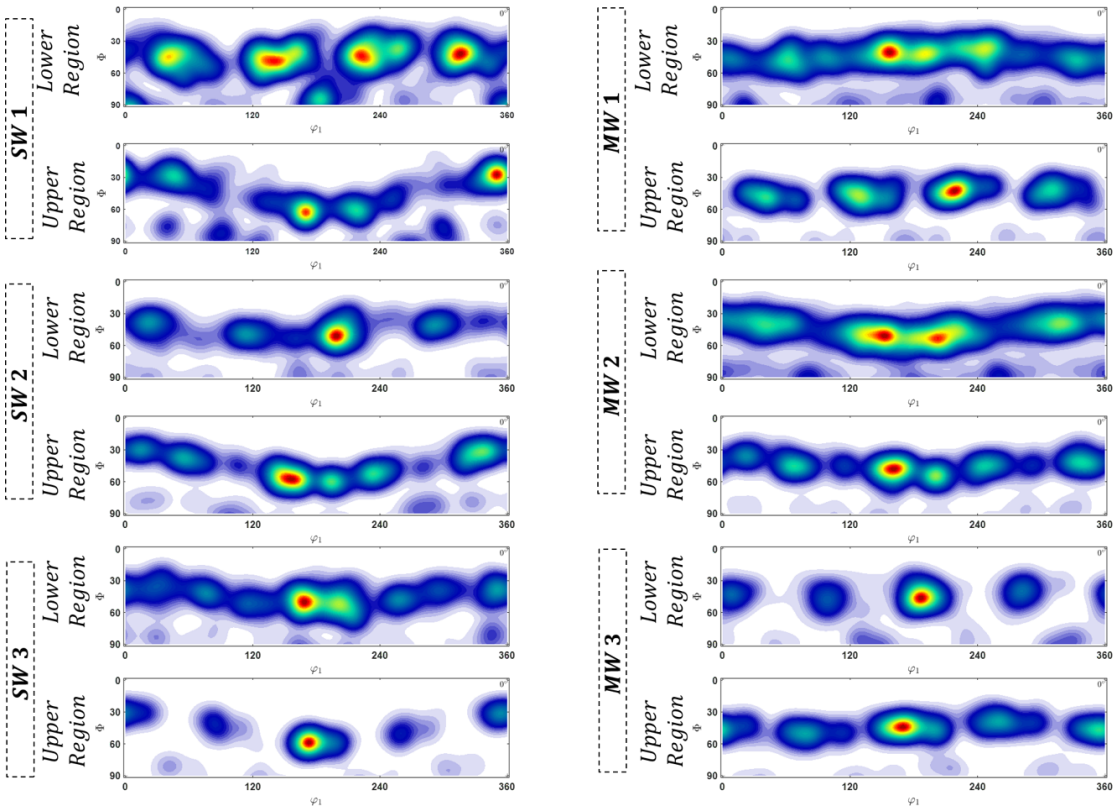

Figure 10: $\phi_2 = 0°$ ODF sections illustrating texture fiber from both lower and upper regions of various SW and MW samples. The primary fiber, $\langle 01\bar{1}2 \rangle_\alpha$ is located at $\phi_2 \approx 42°$, whereas the secondary fiber is present at $\phi_2 \approx 90°$

3.4. Simulation Results

3.4.1. Model Validation

The hardening parameters of the VPSC model were optimized to accurately reproduce the experimental tensile stress–strain curves obtained from the SW specimen across multiple loading directions, achieving an R^2 value greater than 0.90. As shown in Figure 12a, the optimized model provides an excellent fit to the experimental data, confirming the accuracy of the model validation. The optimized values of the hardening parameters are listed in Table 2. The accuracy of the applied VPSC model is further assessed by

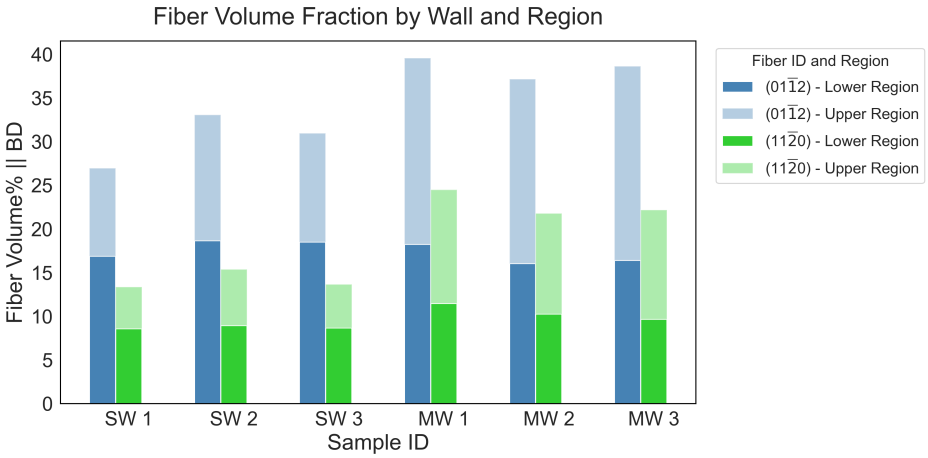

Figure 11: Variation of texture fiber volume with height in various SW and MW specimens.

comparing the predicted texture with the texture obtained from the tensile specimens post-fracture. EBSD scans was performed away from the necked region that exhibited approximately 5% deformation. The scan area was chosen to minimize the effect of strain localization near the necking region while highlighting the influence of strain on texture evolution. As shown in Figure 12c, the predicted and experimental textures when represented by $(0001)_\alpha$ and $(11\bar{2}0)$ pole figures exhibited strong agreement, further supporting the accuracy of the model predictions. However, the predicted texture showed slightly lower intensities compared to the experimental measurements.

Table 2: The optimized Voce hardening parameters used in VPSC modeling

Slip Systems	Hardening Parameters			
	τ_0	τ_1	θ_0	θ_1
Prismatic	400	205	140	-150
Basal	282	126	95	-150
Pyr. $\langle c+a \rangle^+$	635	700	813	-150
Pyr. $\langle a \rangle$	491	408	330	-150

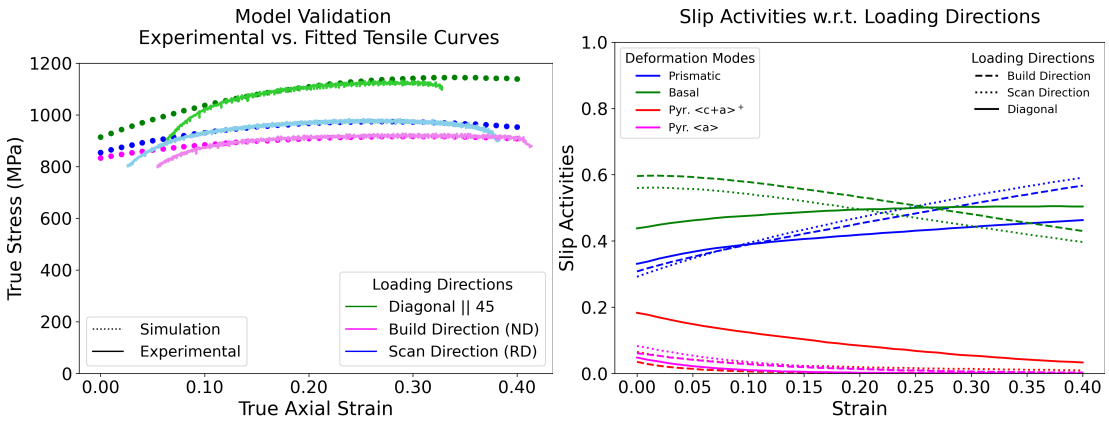

(a)

(b)

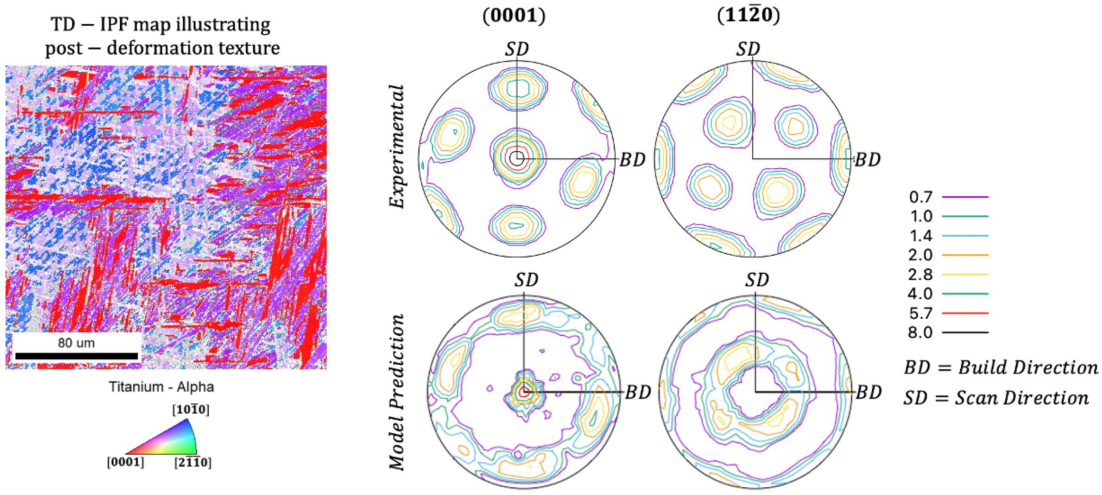

(c)

Figure 12: (a) Plot demonstrating the goodness of the fit between experimental and predicted tensile curves for three tensile directions, *i.e.*, BD, SD, and diagonal direction between BD and SD; (b) Slip systems activities as a function of deformation level for three tensile directions; (c) Comparison between experimental and predicted texture illustrating the accuracy of model prediction.

The activities of various slip systems are presented in Figure 12b. It reveals that the basal and prismatic slip systems primarily accommodate the accumulated shear during deformation. Furthermore, higher mechanical strength observed when the tensile axis is oriented diagonally between the build direction and the scan direction. This can be

attributed to the reduced activity of the basal slip systems which requires the pyramidal $\langle c{+}a\rangle$ slip to activate to accommodate deformation under this loading direction. Although pyramidal $\langle c + a\rangle$ slip activation is much more unlikely than pyramidal $\langle a\rangle$ slip due to the significantly higher critical resolved shear stress (CRSS) of the former [43], its contribution to deformation becomes substantial, effectively compensating for strain along the $\langle c\rangle$ direction of HCP α unit cell.

3.4.2. Effect of Site-specific Texture on Mechanical Properties

The VPSC modeling framework focuses exclusively on SW specimens to evaluate the influence of site-specific texture on mechanical behavior. This decision is based on the observation that the variation in mechanical properties, evaluated by Vickers hardness, along the build height is more pronounced in SW specimens compared to MW specimens [3]. In MW samples, the mechanical property variation is relatively minor and can be sufficiently explained by changes in α-lath thickness along the wall height. As a result, further modeling of site-specific texture effects in MW specimens is deemed unnecessary. Supporting results for MW samples are provided in the appendix for completeness. For SW, Figure 13a depicts the influence of local texture variations across different wall heights on the mechanical response under tensile loading along the build direction (BD || Z-axis). The model predicts that the bottom region of SW1 specimen should exhibit higher yield and tensile strengths compared to the center and top regions. Conversely, for SW2 and SW3 specimens, the top region is expected to demonstrate superior mechanical strength relative to the lower two sections. These variations are attributed to the relative alignment of the active slip systems with respect to the loading direction. Slip activity analysis further reveals distinct differences in the contribution of individual slip systems across the three regions, leading to the observed mechanical variations. Most of the deformation in tensile loading is accommodated by basal slip, followed by prismatic slip, while pyramidal $\langle a\rangle$ and $\langle c + a\rangle$ systems remain largely inactive, with their activity further diminishing at higher strain levels.

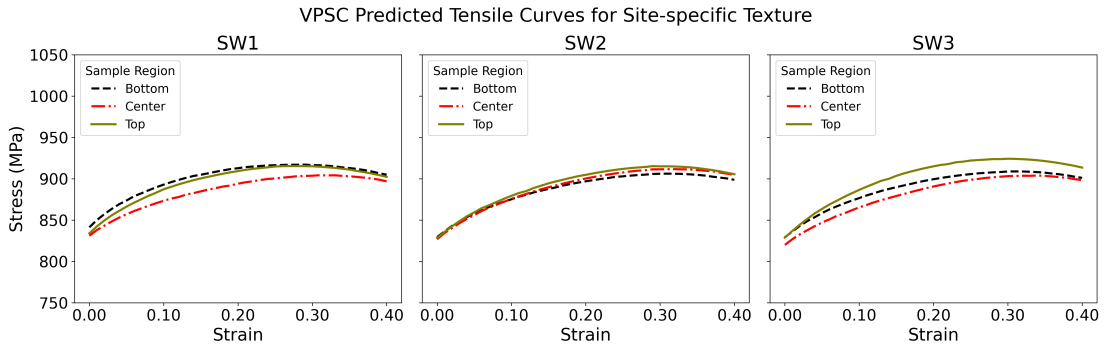

(a)

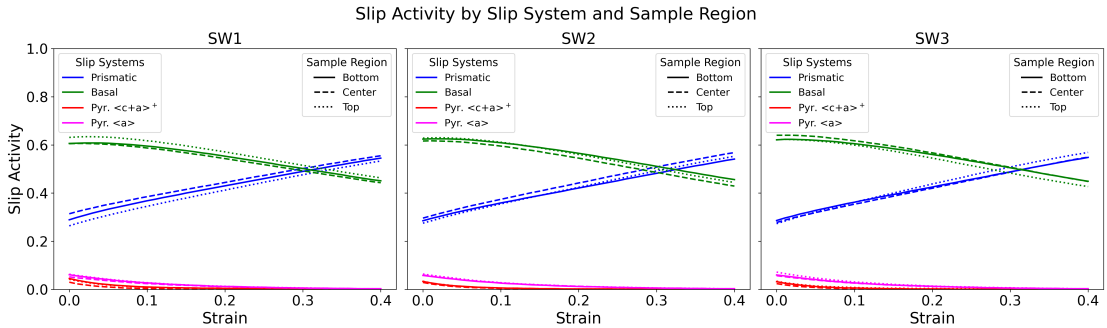

(b)

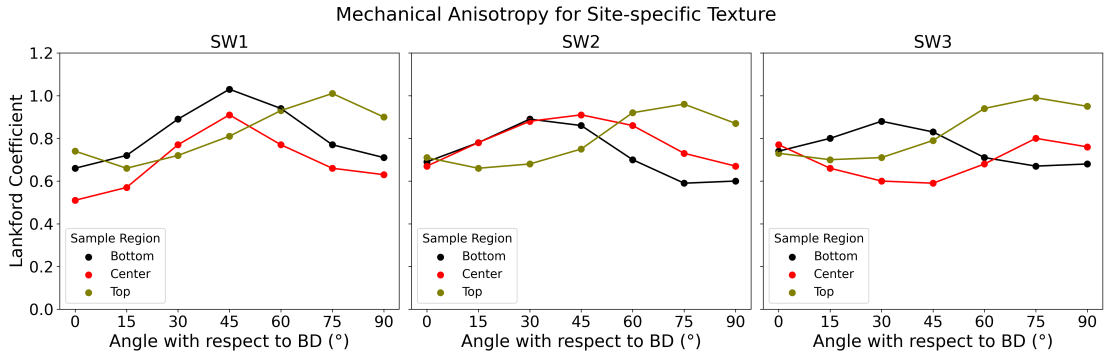

(c)

Figure 13: (a) Effect of site-specific texture on the tensile curves for SW1, SW2, and SW3 specimens; (b) Evolution of slip activities as a function of strain for different regions of SW specimens; (c) Mechanical anisotropy at the bottom, middle, and top sections of SW structures captured from the variation of the Lankford coefficients as a function of loading axis deviation with respect to the build direction.

The evolution of site-specific textures affects not only tensile properties but also mechanical anisotropy within each region. The anisotropy is characterized by the plastic strain ratio, also known as the Lankford coefficient r, defined as the strain ratio in width to thickness [44]. The Lankford coefficient after 10% deformation was predicted using the VPSC subroutine with `IVGVAR = 3`. Simulations were performed under uniaxial tension aplied at 15° increments between the build direction and the scan direction. As shown in Figure 13c, differences in local texture at the bottom, center, and top regions of the SW specimen lead to a distinct evolution of the Lankford coefficient as a function of the loading axes relative to the build direction. In all cases, the predicted Lankford coefficients $r < 1$ which is a quantitative manifestation of mechanical anisotropy and suggest that the crystallographic orientation causes more contraction through thickness than lateral expansion under tensile loading [45]. The pronounced plastic anisotropy in the SW specimen is attributed to the basal texture tilted relative to the build direction. This also highlights the anisotropic response of HCP polycrystals sensitive to both the orientation and intensity of the basal pole. These findings are consistent with trends reported in the literature [46, 47, 48].

4. Discussion

4.1. Effect of Interlayer Delay on Texture Evolution

The intensity of the α texture increases with wall height for all SW structures irrespective of processing conditions, as illustrated in Figure 7a. This can be attributed to the coarsening of β grains, which occurs due to reduced cooling rates at greater heights [3]. Moreover, the α texture becomes progressively stronger across the three SW specimens when comparing the texture intensities of corresponding sections.

This strengthening can be attributed to two main factors: (a) the size of the β grains and (b) variant selection during $\alpha \rightarrow \beta \rightarrow \alpha$ phase transformation, which is driven by thermal cycling through the $\beta_{transus}$ during deposition. In this regard, Obasi *et al.* [49]

investigated the influence of β grain growth on variant selection and texture memory during $\alpha \rightarrow \beta \rightarrow \alpha$ transformation in Ti64 alloy. They reported that the strengthening of α texture during thermal cycling heat treatment is driven by β grain growth and the early nucleation of α phase (*i.e.*, macrozones).

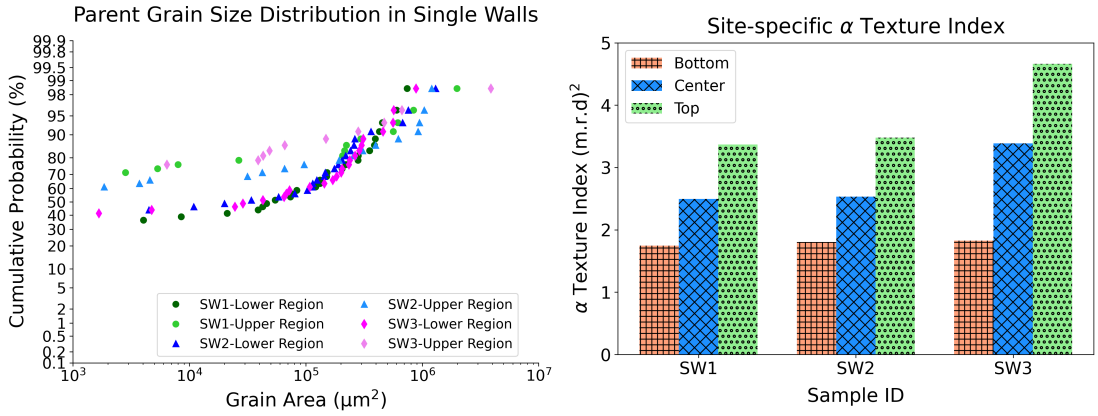

(a) (b)

Figure 14: (a) Cumulative probability distribution of prior β grain area for three SWs. The bottom and top sections represent the entire reconstructed β map for the lower and upper half of the wall as shown in Figure 8; (b) α texture index at the bottom, middle and top sections for various SW specimens.

The β grain size was carried out from the respective reconstructed β maps from 2D grain area, as shown in Figure 14a. The cumulative probability vs. grain area plot for the three SW specimens indicates that the probability of encountering larger β grains increases from SW1 to SW3. This implies that the growth of β grains plays a key role in enhancing the texture intensity with increasing interlayer delay. Furthermore, the comparison of α texture index across the three sections of each wall, as depicted in Figure 14b reconfirms the trend of increasing texture intensity with longer interlayer delay. In this regard, Table 3 summarizes β grain sizes and associated effect on the texture of Ti64 structures fabricated by various AM processes. However, macrozone analysis for SW specimens, as reported in our previous work [18], does not provide any strong evidence of increasing density that correlates with increased interlayer delay.

Another plausible explanation for the progressive increase in texture strength from SW1 to SW3 is related to the reduced number of thermal cycles experienced by each layer through the $\beta_{transus}$ during the layer-by-layer deposition process. This reduction is driven by a lower heat accumulation from prolonged interlayer delays which influences the cooling rates across the wall heights and in turn regulates the heat accumulation during deposition [3]. A longer interlayer delay allows residual heat to dissipate before a new layer is deposited, thereby reducing the number of $\alpha \rightarrow \beta \rightarrow \alpha$ thermal cycles through $\beta_{transus}$ experienced by a layer under subsequent continued deposition. Since each $\alpha \rightarrow \beta \rightarrow \alpha$ transformation offers 72 possible variant selections [49], and a reduced number of thermal cycles per layer is expected to promote stronger α texture development from the formation of fewer α variants. An increased interlayer delay reduces heat accumulation and, consequently, the frequency of $\alpha \rightarrow \beta \rightarrow \alpha$ phase transformations per layer. The resulting decrease in thermal cycling from SW1 to SW3 therefore reinforces the strength of α texture evolution.

Table 3: Summary of previously reported β grain sizes and their influence on the texture evolution in various Ti64 parts fabricated using different AM processes.

Reference	**AM Process**	**Sample Geometry**	**Reported Prior-β Grain Size**	**Effect on Texture**
Neikter *et al.* [27, 50]	PBF: SLM & EBM; DED: LMpD, LMwD, SMD	PBF: block; DED: thin-wall	PBF: ~87–93 μm width (columnar); DED: ~200 μm to ~4 mm width	PBF: finer β grains yielded refined α-lath colonies; DED: coarse β grains (up to several mm) promoted epitaxial growth and strong <001> texture.
Sangid *et al.* [51]	EBM	Tensile coupons	Columnar β grains hundreds of μm thick; ~0.5–1 mm long	Columnar β grains led to a strong <001> α texture; crystal plasticity modeling confirmed influence on anisotropic strength. Texture persisted after HIP.
Yoon *et al.* [52]	Laser DED with/without pulsed laser (PL)	30 mm-tall thin wall	Conventional: ~1297 μm; PL-DED: ~549.6 μm (refined)	Pulsed laser refined the β grain structure, weakening the texture. β-phase texture intensity (MUD) dropped from 16 to 7.7.
Yuan *et al.* [53]	Laser Wire DED with/without ultrasound	Multi-walls	Without ultrasound: coarse columnar β grains; with ultrasound: finer β grains (width reduced)	Ultrasound disrupted epitaxial β growth, producing finer β grains and a more isotropic α texture. Acoustic cavitation confirmed as refinement mechanism.
Sahu *et al.* [54]	WAAM with/without Ultrasonic Impact Peening	Wall ~15 cm tall	As-deposited: cm-scale β grains; With UIP: refined to $\langle$1 cm	UIP induced recrystallization, breaking up columnar grains and weakening the strong <001> texture. Resulted in reduced anisotropy.
Baufeld *et al.* [24]	WAAM	Thin wall ($\rangle$100 mm tall)	Transition from equiaxed (base) to columnar (top); grains several mm long	Columnar β grains generated strong <100> texture along build direction. Grain coarsening with height reinforced aligned α colonies and build anisotropy.

PBF = Powder bed fusion; SLM = Selective laser melting; EBM = Electron beam melting; DED = Directed energy deposition; LMpD= Lase metal powder deposition; LMwD= Laser metal wire deposition; SMD= Shaped metal deposition; WAAM = Wire arc additive manufacturing; HIP= hot isostatic pressing

4.2. Effect of Scan Strategy on Texture Evolution

The three scan strategies employed in case of MW Ti64 specimens show no clear correlation with the strength of either β or α texture. This can be attributed to the similar thermal histories experienced by all MW samples, irrespective of the scan strategy used during fabrication. The corresponding thermal history data for these samples is provided in the appendix.

4.3. Origin of α Fiber

Figure 15a represents the location of poles corresponding to various crystallographic planes of BCC β phase within a standard $(100)_\beta$ stereogram. The $(100)_\beta$ pole is positioned at the center of the stereogram and corresponds to the β grains oriented parallel to the build direction. $(110)_\beta$ poles, marked in green, are located at 45° and 90° from BD, while four $(111)_\beta$ poles, highlighted in blue, are situated at 54.7° from it. Figure 15b similarly presents standard $(11\bar{2}0)_\alpha$ stereogram, where $(0001)_\alpha$ poles are located at the periphery (indicated by the green circle), and one of the three $(11\bar{2}0)_\alpha$ poles lies at 54.7° (marked by the black circle) from the BD. Comparing Figures 15a & 15b, the locations of the close-packed poles in $(0001)_\alpha$ and $(11\bar{2}0)_\alpha$ stereograms correspond to one of the six $(110)_\beta$ poles (green circle) and one of the four $(111)_\beta$ poles (black circle) following the Burgers orientation relationship [55]. Preferred selection of certain α variants further drives $(11\bar{2}0)_\alpha$ pole towards BD (indicated by the green arrow in Figure 15b), leading to the formation of a strong $\langle 11\bar{2}0\rangle_\alpha \parallel$ BD texture fiber.

Figure 15c represents $(01\bar{1}2)_\alpha$ stereogram, with $(0001)_\alpha$ poles and one of the three $\langle 11\bar{2}0\rangle_\alpha$ poles lying at 45° (red circle) and 54.7° (blue circle), respectively from BD. These close-packed poles again align with one of the six $(110)_\beta$ poles (red circle) and one of the four $(111)_\beta$ poles (blue circle) from Figure 15a according to the Burgers orientation relationship. This specific α variant thereafter aligns $(01\bar{1}2)_\alpha$ poles parallel to BD (shown by the dark blue arrow in Figure 15c) and results in the formation of fibers like $\langle 01\bar{1}2\rangle_\alpha \parallel$

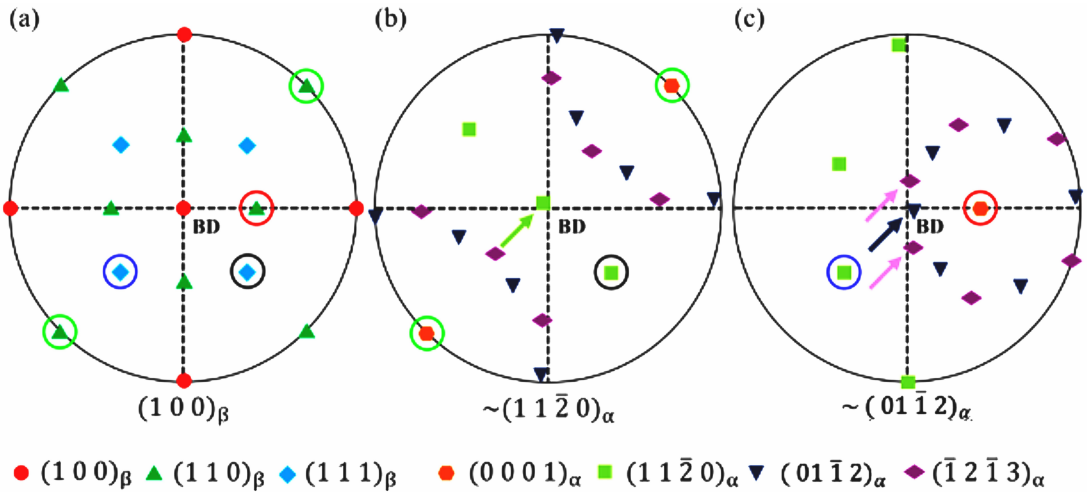

Figure 15: (a) Standard $(100)_\beta$ stereogram illustrates the locations of $(100)_\beta$, $(110)_\beta$, and $(111)_\beta$ poles; (b) $(11\bar{2}0)_\alpha$ stereogram showing the positions of $(0001)_\alpha$ and $(11\bar{2}0)_\alpha$ poles; (c) $(01\bar{1}2)_\alpha$ stereogram showing the locations of $(0001)_\alpha$, $(01\bar{1}2)_\alpha$, and $(\bar{1}2\bar{1}3)_\alpha$ poles. The center of these stereograms coincide with BD. The corresponding color coding for different orientations is provided alongside.

BD. Since the volume fractions of fibers viz. $\langle 01\bar{1}2\rangle_\alpha \parallel$ BD and $(11\bar{2}0)_\alpha \parallel$ BD vary between different SW and MW specimens, it can be inferred that α variant selection also differs for them. Additionally, the volume fraction of any specific fiber changes with wall height, thereby suggesting a distinct difference in α variant selection between the lower and upper regions of any SW or MW specimen. Furthermore, the presence of a strong $\langle 01\bar{1}2\rangle_\alpha \parallel$ BD fiber, represented by $(0001)_\alpha$ poles $\sim 45°$ from build direction, indicates that $(110)_\beta$ planes inclined by $45°$ from BD are preferentially selected in $\beta \rightarrow \alpha$ phase transformation.

4.4. Effect of Texture on Mechanical Properties

The standard stereograms shown in Figure 16 illustrate the orientations of the basal, prismatic, and pyramidal slip systems relative to various texture fibers aligned parallel to BD, *e.g.*, $\langle\bar{1}2\bar{1}3\rangle_\alpha$, $\langle 01\bar{1}2\rangle_\alpha$, and $\langle 11\bar{2}0\rangle_\alpha$. When tensile loading is applied along BD

(*i.e.,* parallel to the fibers), the angular relationships between the tensile axis and the various slip systems can be directly inferred from these stereograms. Similarly, Figure 17 represents orientation of $(\bar{1}2\bar{1}2)_\alpha$, $(01\bar{1}2)_\alpha$, and $(11\bar{2}0)_\alpha$ planes corresponding to various texture fibers aligned along BD within the HCP unit cell. These orientations are used to calculate the Schmid factor (SF), which determines the resolved shear stress in each slip system. Schmid factor calculations thereby enable the prediction of active slip systems and provide insight into the material's deformation behavior under uniaxial loading.

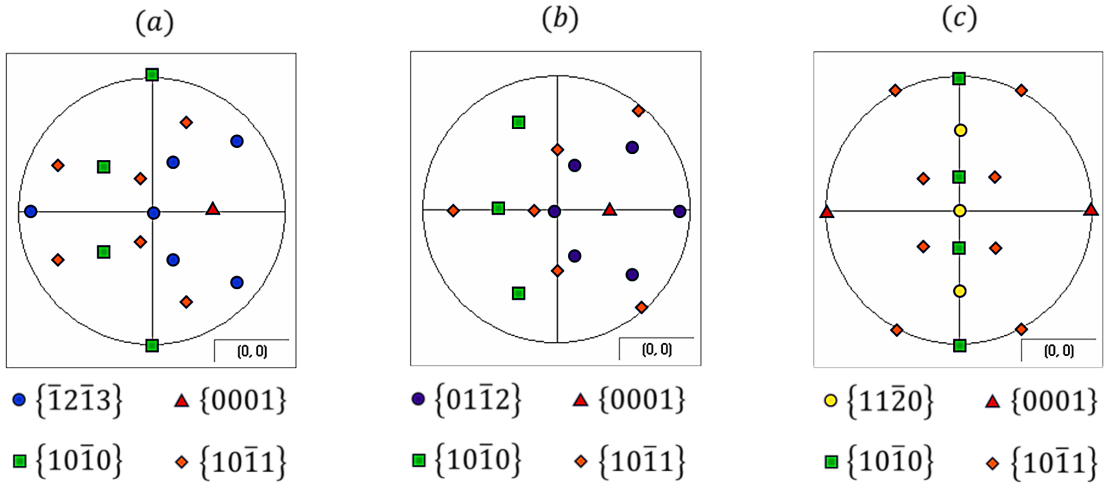

Figure 16: The pole figures demonstrating orientations of basal, prismatic and pyramidal slip systems with respect to $\langle\bar{1}2\bar{1}3\rangle$, $\langle 10\bar{1}2\rangle$, and $\langle 11\bar{2}0\rangle$ fibers in (a), (b), and (c) respectively. These fibers are oriented parallel to the build direction which is aligned with the z-axis located at the center of the pole figures.

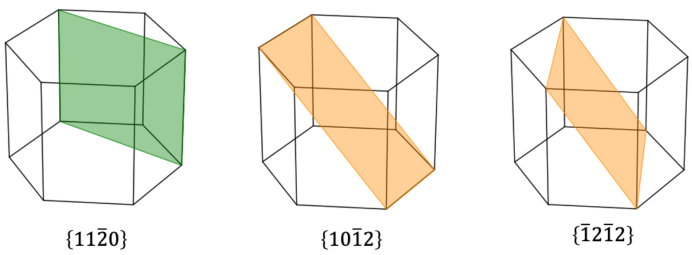

Figure 17: The orientations of $\{11\bar{2}0\}$, $\{10\bar{1}2\}$, and $\{\bar{1}2\bar{1}2\}$ planes in the unit cell

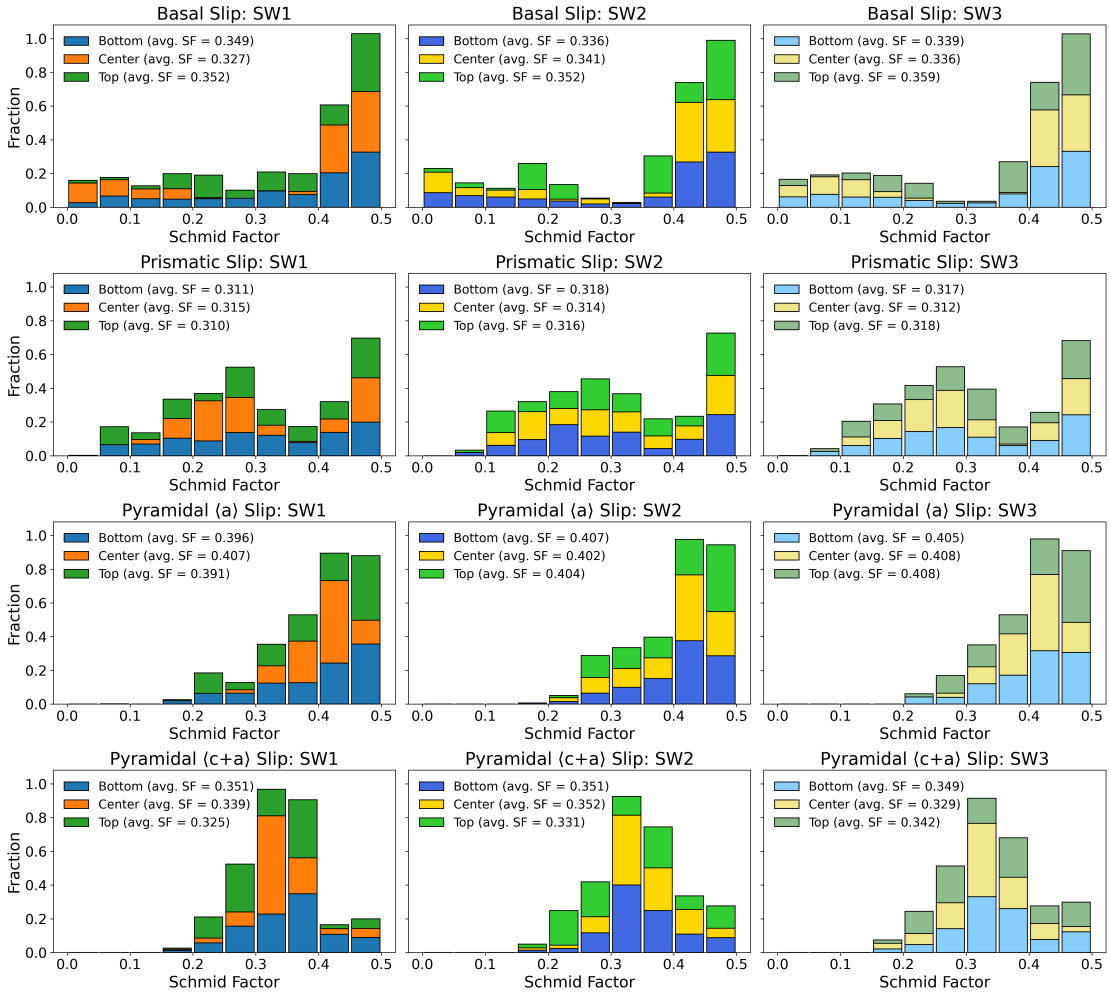

Figure 18: Distributions of Schmid factors for three regions from various SW samples (SW 1, SW 2, and SW 3) with respect to basal, prismatic, pyramidal $\langle a \rangle$ and pyramidal $\langle c + a \rangle$ slip systems

The variation in tensile properties between the bottom, center, and top regions within SW specimens is primarily attributed to differences in site-specific texture. Figure 18 presents the distribution of SF for the three regions in case of SW1, SW2, and SW3, considering basal, prismatic, pyramidal $\langle a \rangle$, and pyramidal $\langle c + a \rangle$ slip systems. The SF distributions differ noticeably among the bottom, center, and top regions within a SW specimen for all possible slip systems mentioned above. The variations in the yield strength observed in VPSC simulations (Figure 13a) across different wall heights can be

directly linked to the site-specific differences in SF. For instance, the center region of SW1 exhibits the lowest yield strength, which correlates to the lower average basal SF compared to the bottom and top regions. It is important to note that the strain hardening behavior cannot be fully explained by the initial Schmid factors alone since it is also influenced by other complex factors like grain reorientation and interactions among slip systems during deformation. The VPSC model however incorporates these effects while fitting the experimental stress-strain curves. The evolution of slip system activity (Figure 13b) therefore helps explain the differences in hardening behavior among various regions for different SW specimens.

5. Conclusions

The site-specific texture in LHW-DED Ti64 SW and MW specimens was investigated using a large-scale EBSD characterization. The effect of this location-dependent texture on the mechanical behavior was also evaluated by developing a polycrystal plasticity based on the VPSC framework. Through the assessment of crystallographic texture and its effect on mechanical behavior, the following conclusions were drawn from this work.

i. The texture strength of the α and β phases increases with increasing height along build direction, mainly due to the coarsening of the β grains with wall height. An increase in interlayer delay was found to enhance α as well as β texture strength in SW specimens. However, in this study, no clear effect of scan strategies on texture strength was observed.

ii. The reconstructed β map revealed the presence of a strong cube texture in the SW and MW samples. The BD || $(100)_\beta$ texture component exhibited its highest intensity at the center of the SW specimens, while in the MW specimens, the maximum strength was observed at the top.

iii. Two α fibers, namely $\langle 01\bar{1}2\rangle_\alpha$ || BD and $\langle 11\bar{2}0\rangle_\alpha$ || BD were observed in SW as

well as MW samples. The primary fiber seen in these walls was $\langle 01\bar{1}2\rangle_\alpha$.

iv. VPSC modeling of the mechanical response revealed that variations in site-specific texture have a relatively minor influence on the tensile properties and anisotropy of Ti64 walls. Under uniaxial tensile loading, deformation was dominated by basal and prismatic slip systems.

Acknowledgments

This work was supported by the Quality Made program led by Lockheed Martin under prime contract N00014-18-C-1026 from the Office of Naval Research. Edward Pierson and Glynn Adams are thanked for fruitful discussions. Furthermore, the authors also thank the MTEX support team (Prof. Frank Niessen from Technical University of Denmark and Prof. Azdiar A. Gazder from University of Wollongong) for providing support with MTEX ORTools. Mark Noakes, Andrzej Nycz, William Carter from Oak Ridge National Laboratory, and Samuel Marra, JP H. Paul and Timothy Novik from Lincoln Electric are thanked for executing the builds and providing samples.

Data Availability

Data will be made available on request.

Appendix A

Figures 19a–c present Vickers hardness maps for the three MW samples, illustrating the spatial distribution of hardness across both wall height and width. The similarity in hardness patterns across all samples suggests that differences in scan strategy have minimal influence on the resulting mechanical properties. Figure 19d further depicts the variation in hardness along the wall height, revealing a consistent decreasing trend in all three MWs. Given the comparable hardness profiles across the samples, the variation in α-lath thickness is shown only for MW3 to emphasize the relationship between microstructural changes and mechanical properties with increasing wall height.

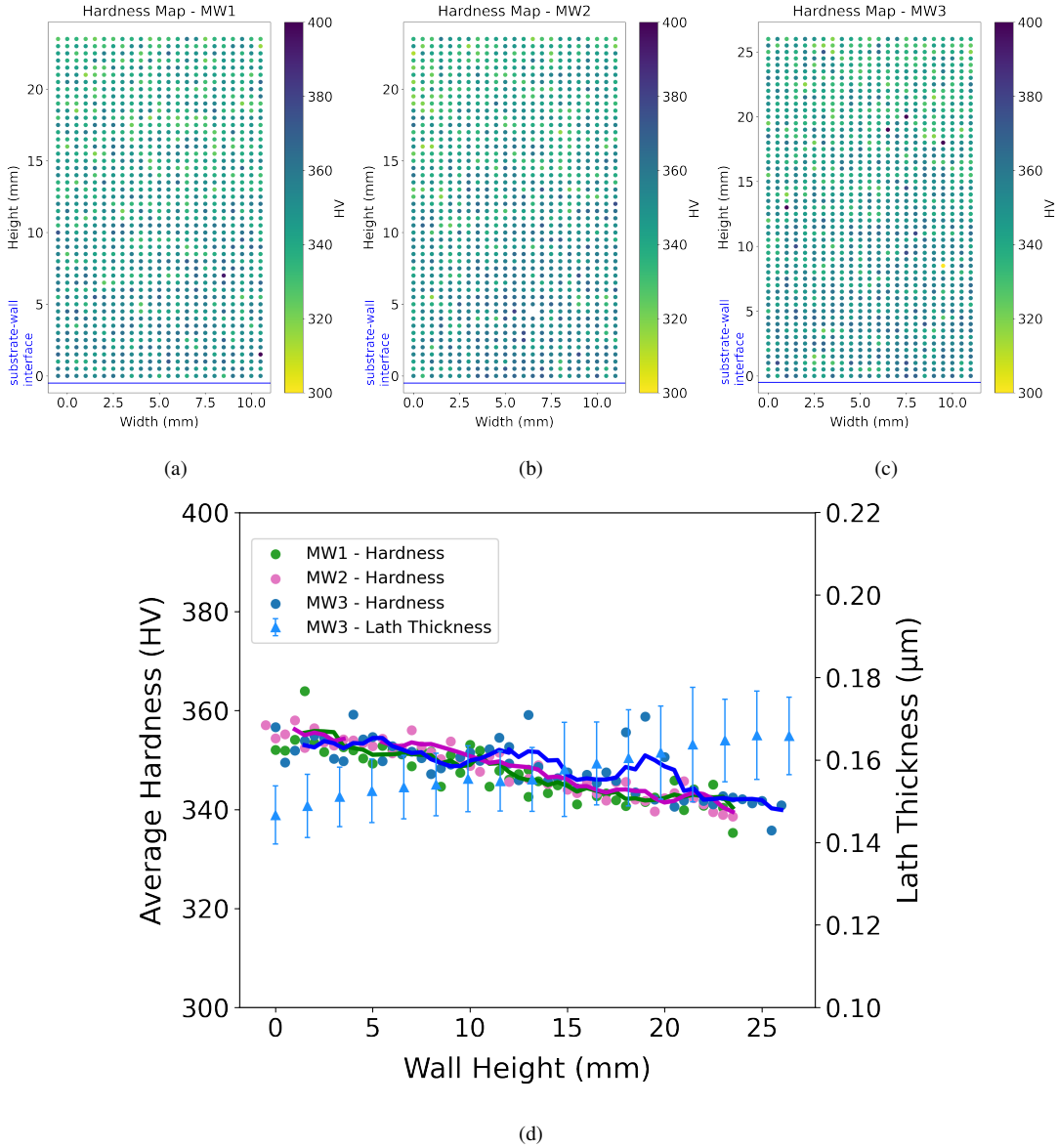

Figure 19: (a–c) Vickers hardness maps of the three MW samples, showing the spatial distribution of hardness across wall height and width; (d) Hardness variation along the wall height for all three MWs is plotted. For MW3, the corresponding variation in α-lath thickness is included to highlight the correlation between microstructural evolution and mechanical properties along the wall height.

Appendix B

For the MW samples, detailed thermal histories were obtained using in situ pyrometer measurements, which record the melt pool temperature as well as temperatures

approximately 38 mm ahead of the melt pool (leading pyrometer) and 38 mm behind it (trailing pyrometer). The thermal profiles illustrated in Figure 20 clearly indicate that all MW specimens experienced nearly identical thermal histories, regardless of the scan strategy employed.

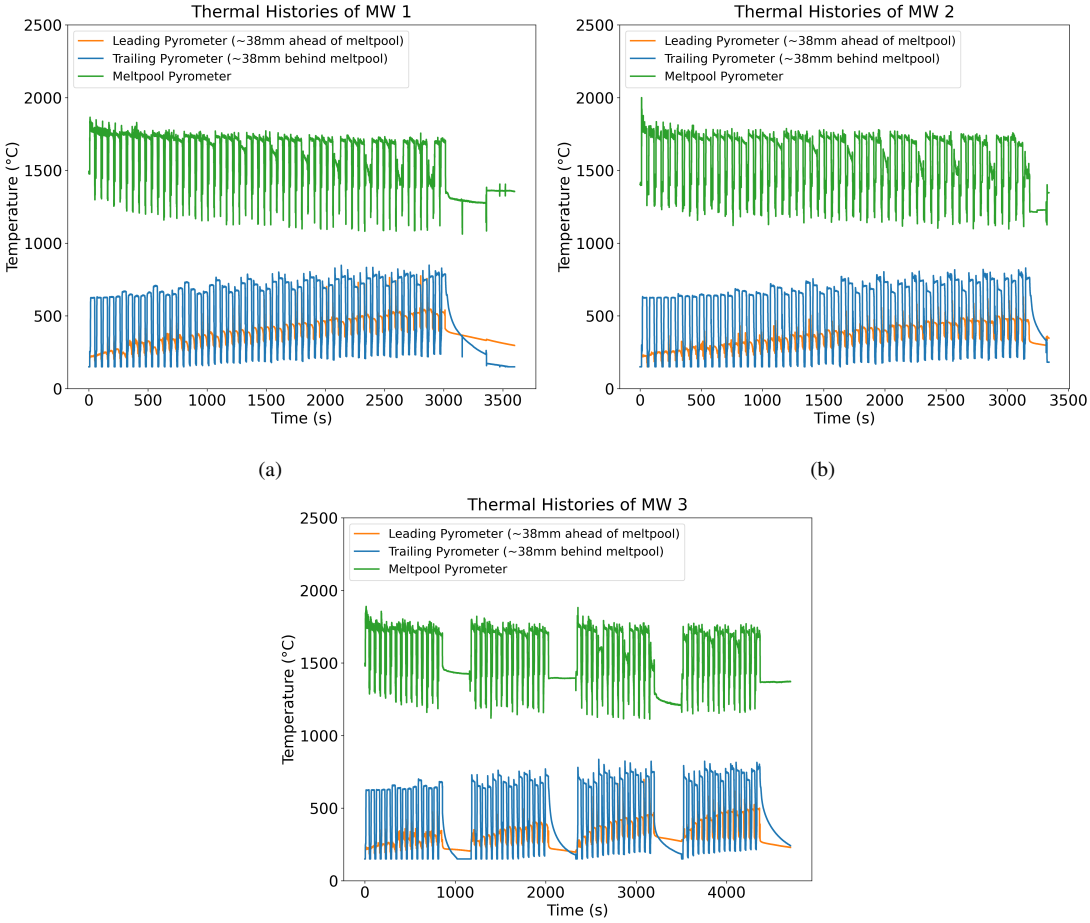

Figure 20: (a-c) In situ temperature histories of MW1, MW2, and MW3 captured using pyrometers.

References

[1] I. Gibson, D. Rosen, B. Stucker, M. Khorasani, D. Rosen, B. Stucker, M. Khorasani, Additive Manufacturing Technologies, Vol. 17, Springer, 2021.

[2] D. Herzog, V. Seyda, E. Wycisk, C. Emmelmann, Additive manufacturing of metals, Acta Materialia 117 (2016) 371–392.

[3] R. Halder, P. C. Pistorius, S. Blazanin, R. P. Sardey, M. J. Quintana, E. A. Pierson, A. K. Verma, P. C. Collins, A. D. Rollett, The Effect of Interlayer Delay on the Heat Accumulation, Microstructures, and Properties in Laser Hot Wire Directed Energy Deposition of Ti-6Al-4V Single-Wall, Materials 17 (13) (2024). doi:10.3390/ma17133307.
URL https://www.mdpi.com/1996-1944/17/13/3307

[4] S. Gorsse, C. Hutchinson, M. Goune, R. Banerjee, Additive manufacturing of metals: a brief review of the characteristic microstructures and properties of steels, Ti-6Al-4V and high-entropy alloys, Science and Technology of Advanced Materials 18 (2017) 584–610. doi:10.1080/14686996.2017.1361305.

[5] H. D. Nguyen, A. Pramanik, A. Basak, Y. Dong, C. Prakash, S. Debnath, S. Shankar, I. Jawahir, S. Dixit, D. Buddhi, A critical review on additive manufacturing of Ti-6Al-4V alloy: microstructure and mechanical properties, Journal of Materials Research and Technology 18 (2022) 4641–4661. doi:https://doi.org/10.1016/j.jmrt.2022.04.055.
URL https://www.sciencedirect.com/science/article/pii/S2238785422005555

[6] D. Waryoba, J. Keist, C. Ranger, T. Palmer, Microtexture in additively manufactured Ti-6Al-4V fabricated using directed energy deposition, Materials Science and Engineering: A 734 (2018) 149–163.

doi:https://doi.org/10.1016/j.msea.2018.07.098.
URL https://www.sciencedirect.com/science/article/pii/S0921509318310323

[7] S. A. Oh, J. W. Aroh, N. L. Lamprinakos, C. A. Chuang, A. N. Bucsek, A. D. Rollett, Martensite decomposition during rapid heating of ti-6al-4v studied via in situ synchrotron x-ray diffraction, Communications Materials 5 (1) (2024) 58. doi:10.1038/s43246-024-00492-6.
URL https://doi.org/10.1038/s43246-024-00492-6

[8] Kelly, S.M. and Kampe, S.L., Microstructural evolution in laser-deposited multilayer Ti-6Al-4V builds: Part I. Microstructural characterization, Metall Mater Trans A 35 (2004) 1861–1867. doi:https://doi.org/10.1007/s11661-004-0094-8.

[9] E. Brandl, A. Schoberth, C. Leyens, Morphology, microstructure, and hardness of titanium (Ti-6Al-4V) blocks deposited by wire-feed additive layer manufacturing (ALM), Materials Science and Engineering: A 532 (2012) 295–307. doi:https://doi.org/10.1016/j.msea.2011.10.095.
URL https://www.sciencedirect.com/science/article/pii/S092150931101197X

[10] X. Wu, J. Liang, J. Mei, C. Mitchell, P. Goodwin, W. Voice, Microstructures of laser-deposited Ti–6Al–4V, Materials & Design 25 (2) (2004) 137–144. doi:https://doi.org/10.1016/j.matdes.2003.09.009.
URL https://www.sciencedirect.com/science/article/pii/S0261306903001742

[11] P. Kobryn, S. Semiatin, Microstructure and texture evolution during solidification processing of Ti–6Al–4V, Journal of Materials Processing

Technology 135 (2) (2003) 330–339, special Issue containing paper from the conference "Research and Development in Net shape Manufactureing". doi:https://doi.org/10.1016/S0924-0136(02)00865-8.
URL https://www.sciencedirect.com/science/article/pii/S0924013602008658

[12] L. Thijs, B. Vrancken, J.-P. Kruth, J. Humbeeck, The influence of process parameters and scanning strategy on the texture in Ti6A14V parts produced by selective laser melting, Materials Science and Technology Conference and Exhibition 2013, MS and T 2013 1 (2013) 21–28.

[13] S. Al-Bermani, M. Blackmore, W. Zhang, I. Todd, The origin of microstructural diversity, texture, and mechanical properties in electron beam melted Ti-6Al-4V, Metallurgical and Materials Transactions A 41 (2010) 3422–3434.

[14] A. Antonysamy, J. Meyer, P. Prangnell, Effect of build geometry on the β-grain structure and texture in additive manufacture of Ti6Al4V by selective electron beam melting, Materials Characterization 84 (2013) 153–168. doi:https://doi.org/10.1016/j.matchar.2013.07.012.
URL https://www.sciencedirect.com/science/article/pii/S1044580313002131

[15] Popov, Vladimir V. and Grilli, Maria Luisa and Koptyug, Andrey and Jaworska, Lucyna and Katz-Demyanetz, Alexander and Klobčar, Damjan and Balos, Sebastian and Postolnyi, Bogdan O. and Goel, Saurav, Powder Bed Fusion Additive Manufacturing Using Critical Raw Materials: A Review, Materials 14 (4) (2021). doi:10.3390/ma14040909.
URL https://www.mdpi.com/1996-1944/14/4/909

[16] Charlotte de Formanoir and Sébastien Michotte and Olivier Rigo and Li-

onel Germain and Stéphane Godet, Electron beam melted Ti–6Al–4V: Microstructure, texture and mechanical behavior of the as-built and heat-treated material, Materials Science and Engineering: A 652 (2016) 105–119. doi:https://doi.org/10.1016/j.msea.2015.11.052.
URL https://www.sciencedirect.com/science/article/pii/S0921509315306420

[17] P. Chandramohan, Laser additive manufactured Ti-6Al-4V alloy: Texture analysis, Materials Chemistry and Physics 226 (2019) 272–278. doi:https://doi.org/10.1016/j.matchemphys.2019.01.035.
URL https://www.sciencedirect.com/science/article/pii/S0254058419300392

[18] R. Halder, S. Sahoo, J. T. Benzing, A. I. Saville, A. D. Rollett, Variant selection and macrozone in Ti-6Al-4V walls during laser hot wire direct energy deposition, Journal of Materials Research and Technology 33 (2024) 8289–8305. doi:https://doi.org/10.1016/j.jmrt.2024.11.061.
URL https://www.sciencedirect.com/science/article/pii/S2238785424025894

[19] S. Liu, Y. C. Shin, Additive manufacturing of Ti6Al4V alloy: A review, Materials & Design 164 (2019) 107552. doi:https://doi.org/10.1016/j.matdes.2018.107552.
URL https://www.sciencedirect.com/science/article/pii/S026412751830916X

[20] N. Biswas, J. Ding, V. K. Balla, D. Field, A. Bandyopadhyay, Deformation and fracture behavior of laser processed dense and porous Ti6Al4V alloy under static and dynamic loading, Materials Science and Engineering: A 549 (2012) 213–221.

[21] M. Strantza, R. Vafadari, D. De Baere, B. Vrancken, W. Van Paepegem, I. Vandendael, H. Terryn, P. Guillaume, D. Van Hemelrijck, Fatigue of Ti6Al4V structural health monitoring systems produced by selective laser melting, Materials 9 (2) (2016) 106.

[22] B. E. Carroll, T. A. Palmer, A. M. Beese, Anisotropic tensile behavior of Ti–6Al–4V components fabricated with directed energy deposition additive manufacturing, Acta Materialia 87 (2015) 309–320. doi:https://doi.org/10.1016/j.actamat.2014.12.054.
URL https://www.sciencedirect.com/science/article/pii/S135964541400980X

[23] Simonelli, M. and Tse, Y. and Tuck, C., Effect of the build orientation on the mechanical properties and fracture modes of SLM Ti–6Al–4V., Materials Science and Engineering: A 616 (2014) 1–11.

[24] B. Baufeld, O. Van der Biest, S. Dillien, Texture and Crystal Orientation in Ti6Al4V Builds Fabricated by Shaped Metal Deposition, Metallurgical and Materials Transactions A 41 (2010) 1917–1927. doi:10.1007/s11661-010-0255-x.

[25] S. Sahoo, A. Joshi, V. K. Balla, M. Das, S. Roy, Site-specific microstructure, porosity and mechanical properties of LENS™ processed Ti–6Al–4V alloy, Materials Science and Engineering: A 820 (2021) 141494. doi:https://doi.org/10.1016/j.msea.2021.141494.
URL https://www.sciencedirect.com/science/article/pii/S0921509321007632

[26] A. Pesach, E. Tiferet, S. C. Vogel, M. Chonin, A. Diskin, L. Zilberman, O. Rivin, O. Yeheskel, E. N. Caspi, Texture analysis of additively manufactured Ti-6Al-

4V using neutron diffraction, Additive Manufacturing 23 (2018) 394–401. doi:10.1016/j.addma.2018.08.010.

[27] M. Neikter, Microstructure and texture of additive manufactured Ti-6Al-4V, Luleå University of Technology, 2017.

[28] A. I. Saville, S. C. Vogel, A. Creuziger, J. T. Benzing, A. L. Pilchak, P. Nandwana, J. Klemm-Toole, K. D. Clarke, S. L. Semiatin, A. J. Clarke, Texture evolution as a function of scan strategy and build height in electron beam melted Ti-6Al-4V, Additive Manufacturing 46 (10 2021). doi:10.1016/j.addma.2021.102118.

[29] J. Ciurana, L. Hernandez, J. Delgado, Energy density analysis on single tracks formed by selective laser melting with CoCrMo powder material, The International Journal of Advanced Manufacturing Technology 68 (2013) 1103–1110. doi:10.1007/s00170-013-4902-4.

[30] C. Springer, W. U. Ahmed, Metallographic preparation of titanium, Praktische Metallographie 21 (1984) 200–203.

[31] F. Bachmann, R. Hielscher, H. Schaeben, Texture analysis with mtex–free and open source software toolbox, Solid State Phenomena 160 (2010) 63–68.

[32] F. Niessen, T. Nyyssönen, A. A. Gazder, R. Hielscher, Parent grain reconstruction from partially or fully transformed microstructures in mtex, Journal of applied crystallography 55 (1) (2022) 180–194.

[33] H. J. Bunge, Texture Analysis in Materials Science. London, Boston, Sydney, Wellington, Durban (1982).

[34] C. N. Tome, R. A. Lebensohn, Material Modeling with the Visco-Plastic Self-Consistent (VPSC) Approach: Theory and Practical Applications, Elsevier Series on Plasticity of Materials, Elsevier, 2023.

[35] R. A. Lebensohn, G. R. Canova, A self-consistent approach for modelling texture development of two-phase polycrystals: Application to titanium alloys, Acta Materialia 45 (9) (1997) 3687–3694. doi:10.1016/S1359-6454(97)00067-0.

[36] R. A. Lebensohn, C. N. Tome, A self-consistent anisotropic approach for the simulation of plastic deformation and texture development of polycrystals: Application to zirconium alloys, Acta Metallurgica et Materialia; (United States) 41:9 (9 1993). doi:10.1016/0956-7151(93)90130-K.
URL https://www.osti.gov/biblio/6303142

[37] Jesús Galán López, Crystal plasticity based modelling of the strain rate dependent mechanical behaviour of Ti-6Al-4V, Ph.D. thesis, Ghent University (2014).
URL https://api.semanticscholar.org/CorpusID:139004228

[38] J. D. Eshelby, R. E. Peierls, The determination of the elastic field of an ellipsoidal inclusion, and related problems, Proceedings of the Royal Society of London. Series A. Mathematical and Physical Sciences 241 (1226) (1957) 376–396. arXiv:https://royalsocietypublishing.org/doi/pdf/10.1098/rspa.1957.0133, doi:10.1098/rspa.1957.0133.
URL https://royalsocietypublishing.org/doi/abs/10.1098/rspa.1957.0133

[39] J. Galán-López, P. Verleysen, Simulation of the plastic response of Ti–6Al–4V thin sheet under different loading conditions using the viscoplastic self-consistent model, Materials Science and Engineering: A 712 (2018) 1–11. doi:https://doi.org/10.1016/j.msea.2017.11.070.
URL https://www.sciencedirect.com/science/article/pii/S0921509317315307

[40] O. Zinovieva and A. Zinoviev and V. Ploshikhin, Three-dimensional

modeling of the microstructure evolution during metal additive manufacturing, Computational Materials Science 141 (2018) 207–220. doi:https://doi.org/10.1016/j.commatsci.2017.09.018.
URL https://www.sciencedirect.com/science/article/pii/S0927025617304986

[41] T. DebRoy and H.L. Wei and J.S. Zuback and T. Mukherjee and J.W. Elmer and J.O. Milewski and A.M. Beese and A. Wilson-Heid and A. De and W. Zhang, Additive manufacturing of metallic components – Process, structure and properties, Progress in Materials Science 92 (2018) 112–224. doi:https://doi.org/10.1016/j.pmatsci.2017.10.001.
URL https://www.sciencedirect.com/science/article/pii/S0079642517301172

[42] S. C. Vogel and S. Takajo and M. A. Kumar and E. N. Caspi and A. Pesach and E. Tiferet and O. Yeheskel , Ambient and High-Temperature Bulk Characterization of Additively Manufactured Ti-6Al-4V Using Neutron Diffraction, The Journal of The Minerals, Metals & Materials Society (TMS) 70 (2018) 1714–1722. doi:https://doi.org/10.1007/s11837-018-3038-2.

[43] R. Halder, L. Corallo, P. Verleysen, L. Kestens, A. D. Rollett, Polycrystal plasticity modeling of the anisotropy of Ti-6Al-4V under static & dynamic loadings, Materials Characterization 224 (2025) 115037. doi:https://doi.org/10.1016/j.matchar.2025.115037.
URL https://www.sciencedirect.com/science/article/pii/S1044580325003262

[44] L. Corallo, P. Verleysen, On the Anisotropic Mechanical Response of Ti6Al4V Sheet at High Strain Rates, Key Engineering Materials 926 (2022) 970–979.

[45] F. Schlosser, C. Schwindt, V. Fuster, A. Tommasi, J. Signorelli, Crystallographic Texture Evolution of a Zinc Sheet Subjected to Different Strain Paths, Metallurgical and Materials Transactions A 48 (03 2017). doi:10.1007/s11661-017-4069-y.

[46] C. Li, J. Sun, A. Feng, H. Wang, X. Zhang, C. Zhang, F. Zhao, G. Cao, S. Qu, D. Chen, Active Slip Mode Analysis of an Additively Manufactured Ti-6Al-4V Alloy via In-Grain Misorientation Axis Distribution, Metals 12 (4) (2022). doi:10.3390/met12040532.
URL https://www.mdpi.com/2075-4701/12/4/532

[47] X. Chen, A. Chapuis, W. He, Q. Liu, Importance of basal slip on the plastic deformation behavior of zirconium alloy Zr702, Journal of Nuclear Materials 606 (2025) 155655. doi:https://doi.org/10.1016/j.jnucmat.2025.155655.
URL https://www.sciencedirect.com/science/article/pii/S0022311525000509

[48] H. Wang, Constitutive modeling of hexagonal close packed polycrystals, Ph.D. thesis, McMaster University (2011).

[49] G. Obasi, S. Birosca, J. Quinta da Fonseca, M. Preuss, Effect of β grain growth on variant selection and texture memory effect during $\alpha \rightarrow \beta \rightarrow \alpha$ phase transformation in Ti–6 Al–4 V, Acta Materialia 60 (3) (2012) 1048–1058. doi:https://doi.org/10.1016/j.actamat.2011.10.038.
URL https://www.sciencedirect.com/science/article/pii/S1359645411007439

[50] M. Neikter, P. Åkerfeldt, R. Pederson, M.-L. Antti, Microstructure characterisation of Ti-6Al-4V from different additive manufacturing processes, IOP Conference Series: Materials Science and Engineering 258 (2017) 012007. doi:10.1088/1757-899X/258/1/012007.

[51] M. D. Sangid, A. Nicolas, K. Kapoor, E. Fodran, J. Madsen, Modeling the Role of Epitaxial Grain Structure of the Prior β Phase and Associated Fiber Texture on the Strength Characteristics of Ti-6Al-4V Produced via Additive Manufacturing, Materials 13 (10) (2020). doi:10.3390/ma13102308.
URL https://www.mdpi.com/1996-1944/13/10/2308

[52] Hansol Yoon and Peipei Liu and Yejun Park and Gwanghyo Choi and Pyuck-Pa Choi and Hoon Sohn , Pulsed laser-assisted additive manufacturing of Ti-6Al-4V for in-situ grain refinement, Scientific Reports 12 (2022) 22247. doi:https://doi.org/10.1038/s41598-022-26758-y.

[53] Yuan D and Shao S and Guo C and Jiang F and Wang J. , Grain refining of Ti-6Al-4V alloy fabricated by laser and wire additive manufacturing assisted with ultrasonic vibration, Ultrason Sonochem 73 (2021) 105472. doi:10.1016/j.ultsonch.2021.105472.

[54] V. K. Sahu, R. Biswal, A. Davis, X. Chen, S. Williams, P. Prangnell, β-Grain refinement in WAAM Ti-6Al-4 V processed with inter-pass ultrasonic impact peening, Materialia 38 (2024) 102236. doi:https://doi.org/10.1016/j.mtla.2024.102236.
URL https://www.sciencedirect.com/science/article/pii/S2589152924002333

[55] W. G. Burgers, On The Process of Transition of the Cubic-Body-Centered Modification into the Hexagonal-Close-Packed Modification of Zirconium, Tech. rep. (1934).